

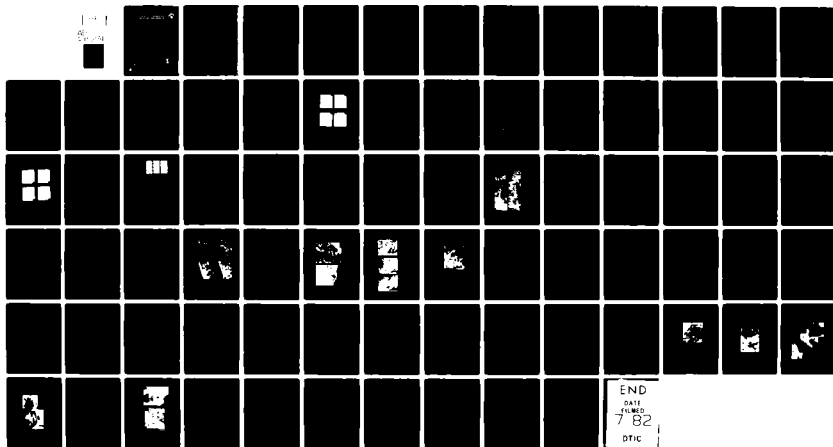
AD-A115 274

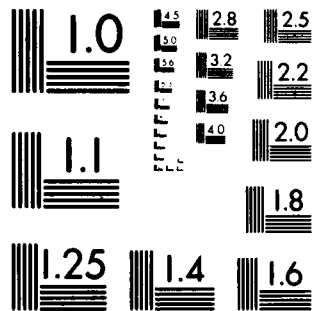
RUTGERS - THE STATE UNIV PISCATAWAY NJ COLL OF ENGIN--ETC F/6 11/6
DETERMINATION OF FATIGUE DAMAGE IN CORROSION-FATIGUED AL-2024-T--ETC(U)
MAY 82 T TAKEMOTO, K L JING, T TSAKALAKOS N00600-77-C-1134

UNCLASSIFIED

DTNSRDC-82/028

NL





MICROCOPY RESOLUTION TEST CHART
NATIONAL BUREAU OF STANDARDS 1963 A

AD A115374

**DAVID W. TAYLOR NAVAL SHIP
RESEARCH AND DEVELOPMENT CENTER**

Annapolis, Maryland 21402

**DETERMINATION OF FATIGUE PROPERTIES IN
CORROSION-FATIGUED A-36 STEEL AND
CYCLED T1-SH-4V ALLOY**

by
T. Takemoto, K.L. Jing, T. Tachibana, and S. Shimizu
College of Engineering, Rutgers University
Piscataway, New Jersey 08854

and
J.R. Egan
David W. Taylor Naval Ship Research and Development Center
Annapolis, Maryland 21402

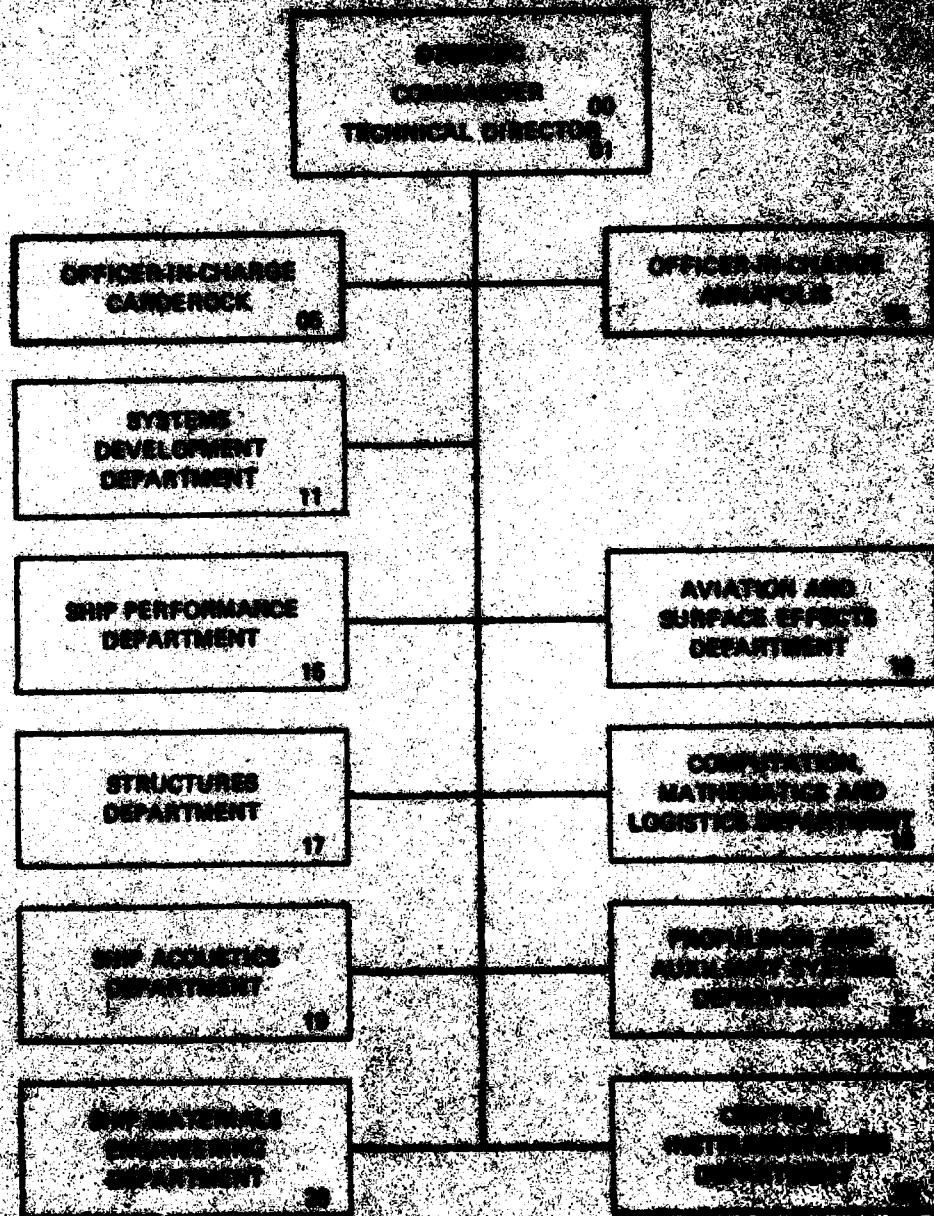
APPROVED FOR PUBLIC RELEASE; DISTRIBUTION UNLIMITED

**SHIP MATERIALS ENGINEERING DEPARTMENT
RESEARCH AND DEVELOPMENT CENTER**

DTIC

5

NAVY ENGINEERING ORGANIZATIONAL CHART



UNCLASSIFIED

SECURITY CLASSIFICATION OF THIS PAGE (When Data Entered)

REPORT DOCUMENTATION PAGE		READ INSTRUCTIONS BEFORE COMPLETING FORM
1. REPORT NUMBER 82/028	2. GOVT ACCESSION NO. AD-A115 274	3. RECIPIENT'S CATALOG NUMBER
4. TITLE (and Subtitle) DETERMINATION OF FATIGUE DAMAGE IN CORROSION- FATIGUED A1-2024-T4 AND CYCLED Ti-6Al-4V ALLOYS		5. TYPE OF REPORT & PERIOD COVERED Research and Development
		6. PERFORMING ORG. REPORT NUMBER
7. AUTHOR(s) T. Takemoto, K.L. Jing, T. Tsakalakos and S. Weissmann (Rutgers University) and I. R. Kramer (DTNSRDC)		8. CONTRACT OR GRANT NUMBER(s) N00600-77-C-1134
9. PERFORMING ORGANIZATION NAME AND ADDRESS Rutgers University and David W. Taylor Naval Ship R&D Center		10. PROGRAM ELEMENT, PROJECT, TASK AREA & WORK UNIT NUMBERS Project Element 61152N Task Area Z0220101 Work Unit 2802-004
11. CONTROLLING OFFICE NAME AND ADDRESS David W. Taylor Naval Ship R&D Center Annapolis, Maryland 21402		12. REPORT DATE May 1982
		13. NUMBER OF PAGES 66
14. MONITORING AGENCY NAME & ADDRESS (if different from Controlling Office)		15. SECURITY CLASS. (of this report) UNCLASSIFIED
		15a. DECLASSIFICATION/DOWNGRADING SCHEDULE
16. DISTRIBUTION STATEMENT (of this Report) APPROVED FOR PUBLIC RELEASE; DISTRIBUTION UNLIMITED.		
17. DISTRIBUTION STATEMENT (of the abstract entered in Block 20, if different from Report)		
18. SUPPLEMENTARY NOTES		
19. KEY WORDS (Continue on reverse side if necessary and identify by block number) X-Ray Diffraction Fatigue Aluminum Silicon		
20. ABSTRACT (Continue on reverse side if necessary and identify by block number) X-ray double crystal diffractometer, transmission and scanning electron microscopy methods were employed to examine the cyclic deformation response of A1-2024-T4 in aqueous corrosive medium and the accrued fatigue damage in Ti-6Al-4V alloys. Special consideration was given to the cyclic response of surface and bulk properties.		

(Continued on Reverse Side)

DD FORM 1473
1 JAN 73EDITION OF 1 NOV 68 IS OBSOLETE
S/N 0102-LF-014-6601

UNCLASSIFIED

SECURITY CLASSIFICATION OF THIS PAGE (When Data Entered)

UNCLASSIFIED

SECURITY CLASSIFICATION OF THIS PAGE (When Data Entered)

(Block 20 Continued)

Cycling Al-2024-T4 in the corrosive medium of 3.5 NaCl solution reduced the fatigue resistance and lowered and even eliminated the endurance limit obtained in air. Application of an anodic potential promoted the decline of fatigue limit. In high cycle corrosion fatigue (HCCF) fatigue life was not determined by the maximum applied stress but rather by the mean cyclic stress. The absence of an overall induced microplasticity at very low applied cyclic stresses, the frequency dependence as well as the observed cathodic polarization effects, suggested that in HCCF of Al-2024-T4 hydrogen embrittlement may be the rate determining process. In low cycle corrosion fatigue (LCCF) of Al-2024-T4, when the largest percentage of life was taken up with crack propagation, the maximum applied stress became the rate determining step for fatigue failure. Similar to previous studies of Al-2024 cycled in air, it was shown that this alloy, when subjected to LCCF, exhibited also a propensity for preferential work-hardening of the surface layer compared to the bulk material. Employing X-ray radiation of different penetration depth the induced excess dislocation density with depth from the specimen surface was investigated as a function of fatigue life. This led to the capability for predicting the accrued damage and life in LCCF of Al-2024-T4.

The effects of precycling and surface removal on the fatigue life and fatigue limit of a Ti-6Al-4V alloy were investigated. It was shown that both the fatigue life and fatigue limit were strongly dependent on the severity of precycling. The fatigue limit lost its significance if the alloy was subjected to a precycling treatment with a high stress amplitude. Cycling with stress amplitude below the fatigue limit after precycling showed a dependence of the logarithmic number of cycles to failure on the fraction of pre-fatigue damage. The interdependence of fatigue life and fatigue limit to precycling history was attributed to microcrack formation, principally restricted to a surface layer of less than 100 μm . Depending on the severity of precycling and on the magnitude of the applied cyclic stress, the fatigue damage could be either partially or totally eliminated by surface removal. The α/β interphase region of the surface layer appeared to offer preferred sites for dislocation pile-ups and crack initiation.

Description For	
1. A	<input checked="" type="checkbox"/>
2. A	<input type="checkbox"/>
3. A	<input type="checkbox"/>
4. A	<input type="checkbox"/>
5. A	<input type="checkbox"/>
6. A	<input type="checkbox"/>
7. A	<input type="checkbox"/>
8. A	<input type="checkbox"/>
9. A	<input type="checkbox"/>
10. A	<input type="checkbox"/>
11. A	<input type="checkbox"/>
12. A	<input type="checkbox"/>
13. A	<input type="checkbox"/>
14. A	<input type="checkbox"/>
15. A	<input type="checkbox"/>
16. A	<input type="checkbox"/>
17. A	<input type="checkbox"/>
18. A	<input type="checkbox"/>
19. A	<input type="checkbox"/>
20. A	<input type="checkbox"/>
21. A	<input type="checkbox"/>
22. A	<input type="checkbox"/>
23. A	<input type="checkbox"/>
24. A	<input type="checkbox"/>
25. A	<input type="checkbox"/>
26. A	<input type="checkbox"/>
27. A	<input type="checkbox"/>
28. A	<input type="checkbox"/>
29. A	<input type="checkbox"/>
30. A	<input type="checkbox"/>
31. A	<input type="checkbox"/>
32. A	<input type="checkbox"/>
33. A	<input type="checkbox"/>
34. A	<input type="checkbox"/>
35. A	<input type="checkbox"/>
36. A	<input type="checkbox"/>
37. A	<input type="checkbox"/>
38. A	<input type="checkbox"/>
39. A	<input type="checkbox"/>
40. A	<input type="checkbox"/>
41. A	<input type="checkbox"/>
42. A	<input type="checkbox"/>
43. A	<input type="checkbox"/>
44. A	<input type="checkbox"/>
45. A	<input type="checkbox"/>
46. A	<input type="checkbox"/>
47. A	<input type="checkbox"/>
48. A	<input type="checkbox"/>
49. A	<input type="checkbox"/>
50. A	<input type="checkbox"/>
51. A	<input type="checkbox"/>
52. A	<input type="checkbox"/>
53. A	<input type="checkbox"/>
54. A	<input type="checkbox"/>
55. A	<input type="checkbox"/>
56. A	<input type="checkbox"/>
57. A	<input type="checkbox"/>
58. A	<input type="checkbox"/>
59. A	<input type="checkbox"/>
60. A	<input type="checkbox"/>
61. A	<input type="checkbox"/>
62. A	<input type="checkbox"/>
63. A	<input type="checkbox"/>
64. A	<input type="checkbox"/>
65. A	<input type="checkbox"/>
66. A	<input type="checkbox"/>
67. A	<input type="checkbox"/>
68. A	<input type="checkbox"/>
69. A	<input type="checkbox"/>
70. A	<input type="checkbox"/>
71. A	<input type="checkbox"/>
72. A	<input type="checkbox"/>
73. A	<input type="checkbox"/>
74. A	<input type="checkbox"/>
75. A	<input type="checkbox"/>
76. A	<input type="checkbox"/>
77. A	<input type="checkbox"/>
78. A	<input type="checkbox"/>
79. A	<input type="checkbox"/>
80. A	<input type="checkbox"/>
81. A	<input type="checkbox"/>
82. A	<input type="checkbox"/>
83. A	<input type="checkbox"/>
84. A	<input type="checkbox"/>
85. A	<input type="checkbox"/>
86. A	<input type="checkbox"/>
87. A	<input type="checkbox"/>
88. A	<input type="checkbox"/>
89. A	<input type="checkbox"/>
90. A	<input type="checkbox"/>
91. A	<input type="checkbox"/>
92. A	<input type="checkbox"/>
93. A	<input type="checkbox"/>
94. A	<input type="checkbox"/>
95. A	<input type="checkbox"/>
96. A	<input type="checkbox"/>
97. A	<input type="checkbox"/>
98. A	<input type="checkbox"/>
99. A	<input type="checkbox"/>
100. A	<input type="checkbox"/>

DTIC
COPY
INSPECTED
2

UNCLASSIFIED

SECURITY CLASSIFICATION OF THIS PAGE (When Data Entered)

TABLE OF CONTENTS

	Page
LIST OF FIGURES	iv
LIST OF TABLES	vii
ABSTRACT	1
INTRODUCTION	2
Part I: Determination of Fatigue Damage in Corrosion Fatigued Al-2024-T4	3
I. EXPERIMENTAL PROCEDURE.	3
A. Specimen Preparation	3
B. Testing Procedure	5
C. Corrosion Fatigue Testing Procedure under Applied Potential . .	7
D. Defect Structure Analysis	7
II. RESULTS	7
A. Uniaxial Tensile Deformation	7
B. Low-Cycle Corrosion Fatigue (LCCF) of Al-2024-T4 Alloy (Batch A) in 3.5 pct NaCl Solution	15
1. Comparison of Fatigue Behavior in Air and in 3.5 pct NaCl Solution	15
2. X-ray Analysis of Identical Grains Subjected to Low Cycle Corrosion Fatigue (LCCF)	15
3. Depth Distribution of Excess Dislocation Density Induced by Corrosion Fatigue	19
4. Determination of Accrued Damage and Failure Prediction by the Nondestructive X-ray Method	22
C. High-Cycle Corrosion Fatigue (HCCF) of Al-2024-T4 Alloy in 3.5 pct NaCl Solution	28
1. Dependence of Corrosion Fatigue Life on Cyclic Stress . . .	28
2. Dependence of $\bar{\sigma}^*$ on Maximum Stress	31
3. Fracture Morphology	33
4. Effect of Applied Potentials on Corrosion Fatigue Life and Endurance Limit	36
III. DISCUSSION	42
A. Low-Cycle Corrosion Fatigue	46
B. High-Cycle Corrosion Fatigue	47
IV. SUMMARY	49
Part II: Determination of Fatigue Damage of Ti-6Al-4V Cycled in Air	50
I. EXPERIMENTAL PROCEDURE	50

	Page
II. RESULTS	51
A. Effect of Pre-Fatigue Damage and Removal of Surface Layer on Fatigue Life	51
B. Dependence of Excess Dislocation Density on Cycling and Depth Distance from Surface	54
C. Slip Morphology and Dislocation Distribution	56
D. Observations on Crack Formation and Crack Initiation Induced by Fatigue	61
III. DISCUSSION AND CONCLUSIONS	61
IV. SUMMARY	64
REFERENCES	65

LIST OF FIGURES

1	- Specimen Configuration of Al-2024-T4 Alloy for Corrosion Fatigue Tests	4
2	- Apparatus for Corrosion Fatigue Tests	6
3	- Dependence of Rocking Curves of Surface Grains on Applied Stress for Al-2024-T4 (Batch B), (a) Undeformed, (b) 138 MPa, (c) 207 MPa and (d) 276 MPa, CrK α_1 radiation; Specimen Rotation = 2 minutes of arc	9
4	- Dependence of Halfwidth on Applied Stress for Al-2024-T4 (Batch B) (a) Change in Halfwidth of Identical Reflecting Grains, (b) Change in Average Halfwidth, $\bar{\beta}$	10
5	- Stress-Strain Curve of Al-2024-T4 (Batch B)	11
6	- Distribution of Halfwidth as a function of Applied Strain for Al-2024-T4 (Batch B). (Intensity Threshold Value = 50.)	12
7	- Effect of Intensity Threshold Value on Average Halfwidth at Various Plastic Strains	14
8	- S-N Curve of Al-2024-T4 (Batch A) for R=0.1 in Air and in 3.5 pct NaCl Solution. f=20 Hz	16
9	- Dependence of Average Halfwidth, $\bar{\beta}$, of the Surface Grains on Number of Fatigue Cycles for Al-2024-T4 (Batch A) in Air and 3.5 pct NaCl Solution, σ_{\max} =276 MPa, R=0.1, f=20 Hz	17

10	- Dependence of Rocking Curves of Surface Grains on Corrosion Fatigue Cycles for Al-2024-T4 (Batch A) in 3.5 pct NaCl Solution at $\sigma_{\max}=276$ MPa, $R=0.1$; (a) Undeformed, (b) 2,500 N (=22 pct N_F), (c) 8,000 N (=71 pct N_F) and (d) 11,100 N (=99 pct N_F), $CrK\alpha_1$ Radiation, Rotation Increment = 3 minutes of arc	18
11	- Dependence of Rocking Curve of Identical Grains on Corrosion Fatigue Cycles. Al-2024-T4 (Batch A), $\sigma_{\max}=276$ MPa, $R=0.1$, 3.5 pct NaCl solution. (a) Details of Rocking Curves at Identical Grains, (b) Halfwidth of Identical Grains	20
12	- Dependence of Average Halfwidth, $\bar{\beta}$, on Depth Distance from Surface for Different Fractions of Corrosion Fatigue Life. Al-2024-T4 (Batch A), $\sigma_{\max}=276$ MPa, $R=0.1$	21
13	- Average Halfwidth as a Function of Fatigue Cycles at Various Maximum Stresses, $R=0.1$, $f=20$ Hz (Batch A). Maximum Stress and X-ray Radiations are indicated	23
14	- Ratios of $\bar{\beta}_{Mo}$ to $\bar{\beta}_{Cr}$ as a function of Fraction of Corrosion Fatigue Life at Various Maximum Stresses, $R=0.1$ (Batch A)	25
15	- Light Micrographs Showing Propagating Cracks. (a) After 20,000 cycles at $\sigma_{\max}=241$ MPa, $R=0.1$, corresponding to Point A in Figure 13. (b) After 11,100 cycles at $\sigma_{\max}=276$ MPa, $R=0.1$, corresponding to Point B in Figure 13	26
16	- Surface and Bulk Dependence of Average Halfwidth on Fraction of Corrosion Fatigue Life. Al-2024-T4 Alloy (Batch A), $\sigma_{\max}=276$ MPa, $R=0.1$	27
17	- Al-2024-T4 (Batch B) in 3.5 pct NaCl Solution, $f=20$ Hz. (a) S-N Curve, $R=0.1$, (b) R-N Curve, $\sigma_{\max}=276$ MPa	29
17(c)	- Goodman's Diagram of Al-2024-T4 (Batch B) in 3.5 pct NaCl Solution, $f=20$ Hz	30
18	- Distribution of Halfwidth at Various Stress Levels and R Values for Corrosion Fatigued Al-2024-T4 (Batch B)	32
19	- Dependence of Critical Halfwidth, $\bar{\beta}^*$, on Applied Maximum Stress for Corrosion Fatigued Al-2024-T4 (Batch B).	34

20	- SEM Fractographs of Al-2024-T4 (Batch B), Cycled at $\sigma_{cyc}=124$ MPa, $\sigma_{mean}=152$ MPa, $f=20$ Hz. (a) Cycled in Air; $N_F=311,500$ cycles, (b) Cycled in 3.5 pct NaCl Solution; $N_F=20,000$ cycles	35
20(c)	- SEM Photographs of Crack Initiation Site (Left) and Crack Tip (Right) of Al-2024-T4 (Batch B) Cycled at $\sigma_{cyc}=124$ MPa, $\sigma_{mean}=152$ MPa, $f=20$ Hz in 3.5 pct NaCl Solution	37
21	- SEM Fractographs of Al-2024-T4 (Batch B) Cycled in 3.5 pct NaCl Solution at $f=20$ Hz. (a) $\sigma_{cyc}=47$ MPa, $\sigma_{mean}=57$ MPa; $N_F=900,000$ cycles. (b) $\sigma_{cyc}=41$ MPa, $\sigma_{mean}=97$ MPa; $N_F=1,062,900$ cycles. (c) $\sigma_{cyc}=41$ MPa, $\sigma_{mean}=235$ MPa; $N_F=969,800$ cycles	38
22	- Effect of Frequency on Crack Formation of Al-2024-T4 (Batch B) Cycled at $\sigma_{cyc}=124$ MPa, $\sigma_{mean}=152$ MPa, $f=0.5$ Hz in 3.5 pct NaCl Solution.	39
23	- Effect of Applied Potential on Current Flow of Al-2024-T4 (Batch B) in 3.5 pct NaCl Solution	40
24	- S-N Curves of Al-2024-T4 (Batch B) in Different Environments for $R=0.1$, $f=20$ Hz	41
25	- Goodman's Diagrams of Al-2024-T4 (Batch B) under Free Corrosion and Applied Anodic Potential in 3.5 pct NaCl Solution	43
26	- R-N Curves of Al-2024-T4 (Batch B) for $\sigma_{max}=276$ MPa under Various Corrosion Potentials in 3.5 pct NaCl Solution, $f=20$ Hz	44
27	- Effect of Applied Potential on Fatigue Life of Al-2024-T4 (Batch B) at Various R Values for $\sigma_{max}=276$ MPa in 3.5 pct NaCl Solution, $f=20$ Hz	45
28	- Effect of Pre-Fatigue Damage and Removal of Surface Layer on Fatigue Life of Ti-6Al-4V. $f=10$ Hz, $R=-1.0$	52
29	- Dependence of Number of Cycles to Failure on Fraction of Pre-Fatigue Damage and on Surface Removal	53
30	- Dependence of Average Lattice Misalignment, $\bar{\beta}$, on (a) Fraction of Fatigue Life and (b) Depth from Surface. $f=10$ Hz, Cyclic Stress= 629 MPa	55
31	- Typical Planar Dislocation Configuration of Surface Layer, Induced by Uniaxial Tensile Deformation; $\epsilon_p=2.7$ pct	57

	Page
32 - Slip Activity in Surface Layer Induced by Uniaxial Tensile Deformation; $\epsilon_p=2.7$ pct	58
33 - Dislocation Configuration of Localized Slip Band in Surface Layer, Induced by Fatigue. Cyclic Stress=629 MPa, $N_F=14,000$ cycles . . .	59
34 - Localized Slip Activity in Surface Layer of α -Phase Showing Contrast Effects Characteristic of Microcracks. Cyclic Stress=629 MPa, $N_F=14,000$ cycles	60
35 - Fracture Surface of Ti-6Al-4V; Cyclic Stress=629 MPa, $N_F=13,000$ cycles, (a) Overall View, I=Crack Initiation Site, (b) Enlarged View of Area S Exhibiting Secondary Cracks	62

LIST OF TABLES

1 - Tensile Properties of Al-2024-T4	8
2 - Minimum Background Intensity for Each Strain Level (Al-2024-T4: Batch B) Data Collecting Time: 10 Seconds	13
3 - Dependence of $\bar{\beta}^*$ on Applied Stress Levels	31

ABSTRACT

X-ray double crystal diffractometer, transmission and scanning electron microscopy methods were employed to examine the cyclic deformation response of Al-2024-T4 in aqueous corrosive medium and the accrued fatigue damage in Ti-6Al-4V alloys. Special consideration was given to the cyclic response of surface and bulk properties.

Cycling Al-2024-T4 in the corrosive medium of 3.5 NaCl solution reduced the fatigue resistance and lowered and even eliminated the endurance limit obtained in air. Application of an anodic potential promoted the decline of fatigue limit. In high cycle corrosion fatigue (HCCF) fatigue life was not determined by the maximum applied stress but rather by the mean cyclic stress. The absence of an overall induced microplasticity at very low applied cyclic stresses, the frequency dependence as well as the observed cathodic polarization effects, suggested that in HCCF of Al-2024-T4 hydrogen embrittlement may be the rate determining process. In low cycle corrosion fatigue (LCCF) of Al-2024-T4, when the largest percentage of life was taken up with crack propagation, the maximum applied stress became the rate determining step for fatigue failure. Similar to previous studies of Al-2024 cycled in air, it was shown that this alloy, when subjected to LCCF, exhibited also a propensity for preferential workhardening of the surface layer compared to the bulk material. Employing X-ray radiation of different penetration depth the induced excess dislocation density with depth from the specimen surface was investigated as a function of fatigue life. This led to the capability for predicting the accrued damage and life in LCCF of Al-2024-T4.

The effects of precycling and surface removal on the fatigue life and fatigue limit of a Ti-6Al-4V alloy were investigated. It was shown that both the fatigue life and fatigue limit were strongly dependent on the severity of precycling. The fatigue limit lost its significance if the alloy was subjected to a precycling treatment with a high stress amplitude. Cycling with stress amplitude below the fatigue limit after precycling showed a dependence of the logarithmic number of cycles to failure on the fraction of pre-fatigue damage. The interdependence of fatigue life and fatigue limit to precycling history was attributed to microcrack formation, principally restricted to a surface layer of less than 100 μm . Depending on the severity of precycling and on the magnitude of the applied cyclic stress the fatigue damage could be either partially or totally eliminated by surface removal. The α/β interphase region of the surface layer appeared to offer preferred sites for dislocation pile-ups and crack initiation.

INTRODUCTION

It has been generally accepted by many investigators that the surface layers of metals and alloys play a special role in fatigue crack initiation.¹⁻⁵

Recent studies⁶⁻⁸ of cycled aluminum crystals and Al-2024 alloys have shown the importance of the increased plastic resistance of the surface layer to deformation and have also demonstrated the special dependence of the dislocation structure in the bulk on the deformation behavior of the surface layer. It was shown that in aluminum alloys cycled in inert media the accrued damage could be determined and the remaining life could be predicted, provided the gradual build-up of the excess dislocation density in the bulk could be measured. This objective was accomplished by carrying out X-ray rocking curve measurements of the grains located in the bulk of the material using MoK_α radiation which penetrated beyond the workhardened surface layer. The results of these studies suggested at once the exploration of the behavior of these alloys when fatigued in hostile environment. Hence, a substantial part of the present investigation may be viewed as a logical extension of the aforementioned fatigue studies⁸ to corrosion fatigue.

Alloys, like 7075 and 2024, have been established in the aerospace industry as the basic aluminum alloys and have been regarded as standards with which new alloys and tempers should be compared.⁹ In the technology of titanium alloys Ti-6Al-4V occupies a similar central position of importance and a number of investigators studying the cyclic response of this alloy have attempted to correlate microstructure to fatigue behavior. Wells and Sullivan¹⁰ and Benson et al.,¹¹ have shown that fatigue cracks were always generated at the surface. Moreover, Benson et al.¹¹ found in mill-annealed Ti-6Al-4V, cycled at 600°F and at room temperature, that early crack initiation ($N_0/N_f \leq 0.14$) occurred in $\text{hcp}\alpha$ -grains by a slip mechanism under all stresses except at those near the fatigue limit. Near the fatigue limit at room temperature the fatigue cracks formed at about $N/N_f \sim 0.4$ at the interface between $\text{hcp}\alpha$ and $\text{bcc}\beta$ grains without detectable slip. Under all conditions Stage I fatigue crack formation occupied 50 to 80 pct of the total life. The observation, however, which is very pertinent to the present investigation, was the fact that the Stage I cracks penetrated only 2 to 4 μm into the specimens. In view of the fact that in this

alloy crack initiation is intimately associated with the surface layer and restricted to a shallow thickness of the surface layer, the study of the mechanical properties and microstructural features of the surface layer takes on a special significance.

The studies presented in this report aim to elucidate the relationship of mechanical and microstructural properties between surface and subsurface layers in corrosion-fatigued Al-2024 and in fatigued Ti-6Al-4V alloys. One of the major objectives is to explore for these alloys the influence of surface layer on the extent of fatigue life.

The studies were divided conveniently into two parts. Part I deals with the determination of the damage induced in corrosion-fatigued 2024 aluminum alloy while Part II deals with the determination of fatigue damage of Ti-6Al-4V cycled in air. Since the cyclic response is highly stress or strain dependent with concomitant expected changes in microstructure, special attention has been given to the low-cycle and high-cycle fatigue response.

Part I: Determination of Fatigue Damage in Corrosion Fatigued Al-2024-T4

I. EXPERIMENTAL PROCEDURE

A. Specimen Preparation

Al-2024 alloy rods were obtained for two different grain sizes. Batch A, which contained the smaller grain size, was fabricated into flat specimens in such a way that the loading axis was along the extruded direction. Batch B having larger grain size was given a grain refining treatment as follows: The rods were annealed at 413°C for 8 hours, followed by furnace cooling (0 treatment). They were, then, cold worked, the reduction of area being about 40%. Flat specimens were machined such that the loading axis was in the longitudinal direction and the large surfaces were normal to the short transverse direction. The specimen configuration is shown in Figure 1. After mechanical polishing, using successively finer grades of emery papers down to 600 grit, the specimens were given a solution heat treatment at 493°C for 2 hours in argon atmosphere, they were water quenched

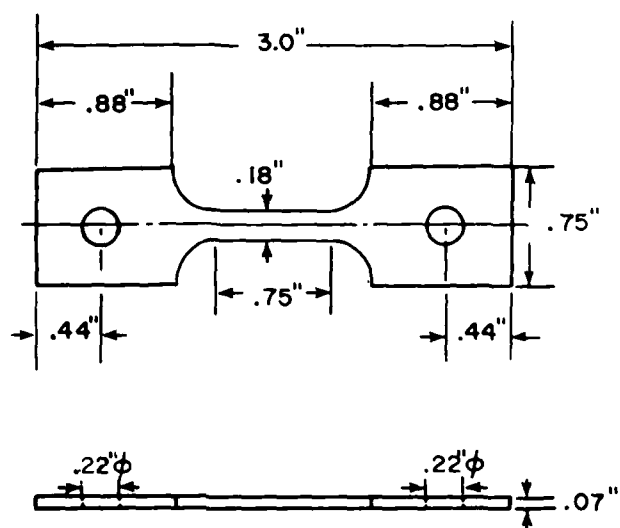


Figure 1. Specimen Configuration of Al-2024-T4 Alloy for Corrosion Fatigue Tests.

and then aged at room temperature for more than 4 days, resulting in the T-4 treatment.

The grain morphology analysis and the grain size measurements were performed with the aid of Keller's etching reagent. The grain sizes of the two batches were determined by the linear intercept technique.

Prior to testing a layer of more than 100 μm thickness was removed from the specimen surface to eliminate the oxidation and contamination effects introduced during the T-4 treatment. Two electro-polishing solutions and operation conditions were used: 25 pct nitric acid and 75 pct methanol with 20 V at -25°C or 20 pct perchloric acid and 80 pct methanol with 20 V at -20°C .

B. Testing Procedure

Static tensile tests were performed in an Instron universal testing machine with strain rate of 0.013 min^{-1} .

Fatigue cycling was carried out in a Tatnell-Krause fatigue machine in air at room temperature and also in a 3.5 pct NaCl solution. An apparatus for corrosion fatigue tests was constructed. It is shown schematically in Figure 2. The grips were made of drill rods, covered with poly-imide in order to eliminate during testing any generation of electric current flow between test specimen and the grips. The upper grip was provided with a universal joint to prevent the specimen from bending when the load was applied. For corrosion fatigue studies a large container of about 1 gallon size was provided with O-ring and was placed between the lower grip and the support plate. The corrosive 3.5 NaCl solution in the container was kept constantly stirred during the test.

Specimens were cycled in tension-tension at a frequency of 20 Hz. The maximum stress, σ_{max} , and the stress ratio, R , were chosen as variables; the latter being defined as the ratio of the minimum stress to the maximum stress.

The incremental fatigue experiments were performed by stepwise cycling. After each fatigue increment, the cycling was interrupted to allow for analyses by X-ray diffraction and optical microscopy. Subsequently, the specimens were remounted in the fatigue machine for the next cycling increment. After eventual failure, each cycling increment was recalibrated

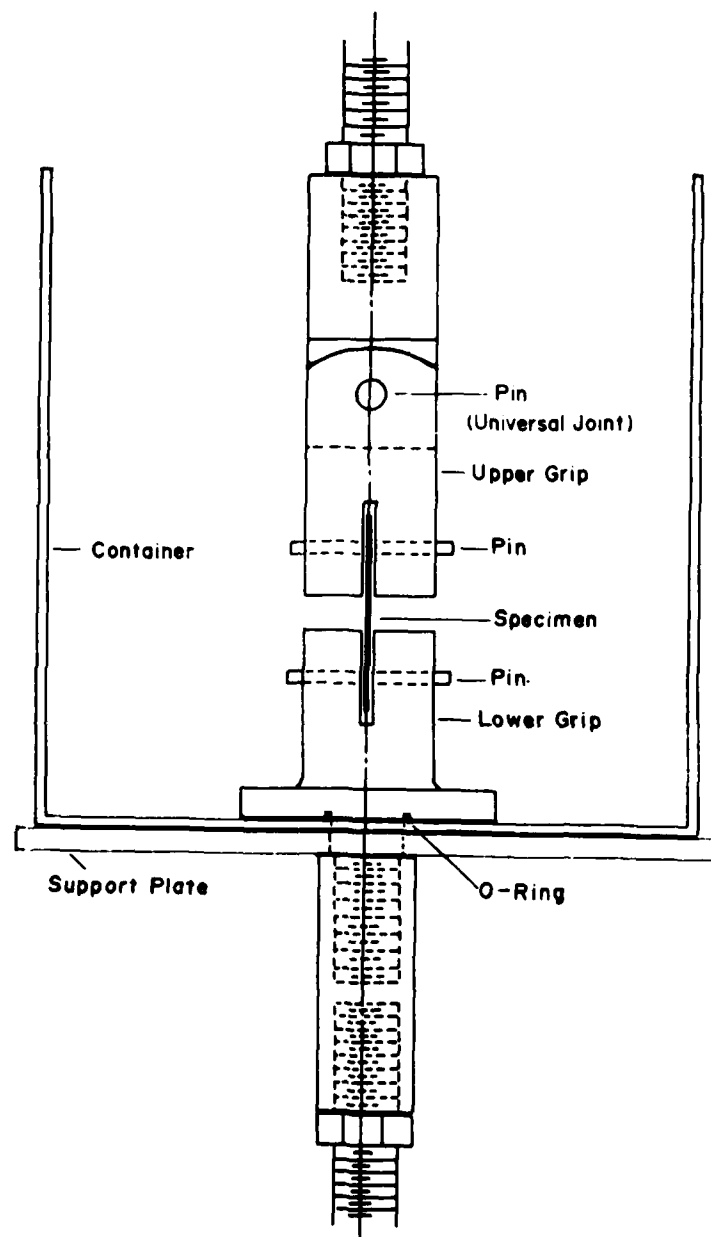


Figure 2. Apparatus for Corrosion Fatigue Tests.

so as to obtain the true fractions of the fatigue life for each specimen.

C. Corrosion Fatigue Testing Procedure under Applied Potential

For closed circuit fatigue studies an external potential was applied to the specimen using a Wenking potentiostat Model LT73. A Standard Calomel electrode, used as reference electrode, and a platinum electrode, used as counter electrode, were fixed at a distance of about 2.5 cm from the specimen. For each test, the specimen was kept initially unstressed until, after applying the external potential, the current flow reached a constant value. When this constant current flow was obtained the specimen was subjected to cycling.

D. Defect Structure Analysis

The double crystal diffractometer (DCD) method for polycrystalline materials^{12,13} was used to analyze the defect structures induced by fatigue and corrosion fatigue cycling, as well as by uniaxial tensile deformation. The rocking curve measurements were carried out as a function of: (a) number of fatigue cycles, (b) depth distance from the specimen surface, and (d) plastic strain. Two techniques of the DCD method were employed: (a) automated film technique and (b) Computer Aided Rocking Curve Analysis (CARCA).^{14,15}

II. RESULTS

A. Uniaxial Tensile Deformation

Uniaxial, monotonic tensile studies of the Al-2024-T4 alloy were carried out and correlated to the X-ray rocking curve measurements. These studies aimed to establish a basis of comparison for subsequent cyclic deformation studies performed in air as well as in a corrosive medium. The tensile properties were measured by straining the specimens at a constant strain rate of 0.013 min^{-1} . The results obtained are given in Table 1.

TABLE 1 - TENSILE PROPERTIES OF Al-2024-T4

Yield Stress	40,000 psi = 276 MPa
Tensile Stress	67,000 psi = 462 MPa
Elongation	19.5%

Rocking curve measurements as a function of the applied stress were carried out to investigate the dependence of the rocking curve halfwidth, β , of the reflecting grains on the tensile properties. The DCD method with film technique was applied. The specimen was held at each stress level for 16 hours before increasing it to the next stress level. Identical reflecting grains could be analyzed, as shown in Figure 3 (#1-5). It can be seen that after stressing at 138 MPa, most reflecting grains retained their angular range of reflection. Some reflecting grains, however, as a result of the applied stress, were rotated out of the reflecting position (for example, A and B in (a)) while reflecting grains, such as C and D, were rotated into the reflecting range.

At 207 MPa, rocking curves of grains exhibited small broadening and at the stress of 276 MPa, which corresponds to the static yield stress, all reflecting grains exhibited large increases in β values. Figure 4(a) shows the dependence of β of some individual reflecting grains on the applied stress and Figure 4(b) represents the average halfwidth, $\bar{\beta}$, of the surveyed grain population as a function of the applied stress. The increase in $\bar{\beta}$, became noticeable at the stress of 207 MPa and at the stress of 276 MPa $\bar{\beta}$ was about 44 pct larger than $\bar{\beta}_0$; the latter being the average halfwidth of the grains of the undeformed specimen. The novel Computer Aided Rocking Curve Analysis (CARCA) system^{14,15} was employed to examine the distribution of the halfwidth as a function of strain. The stress-strain curve of Al-2024-T4 alloy is given in Figure 5 and the rocking curve measurements were carried out at strain levels marked on the stress-strain curve by points. Figure 6 represents the distribution of the values at these different strain levels. It will be noted that the first

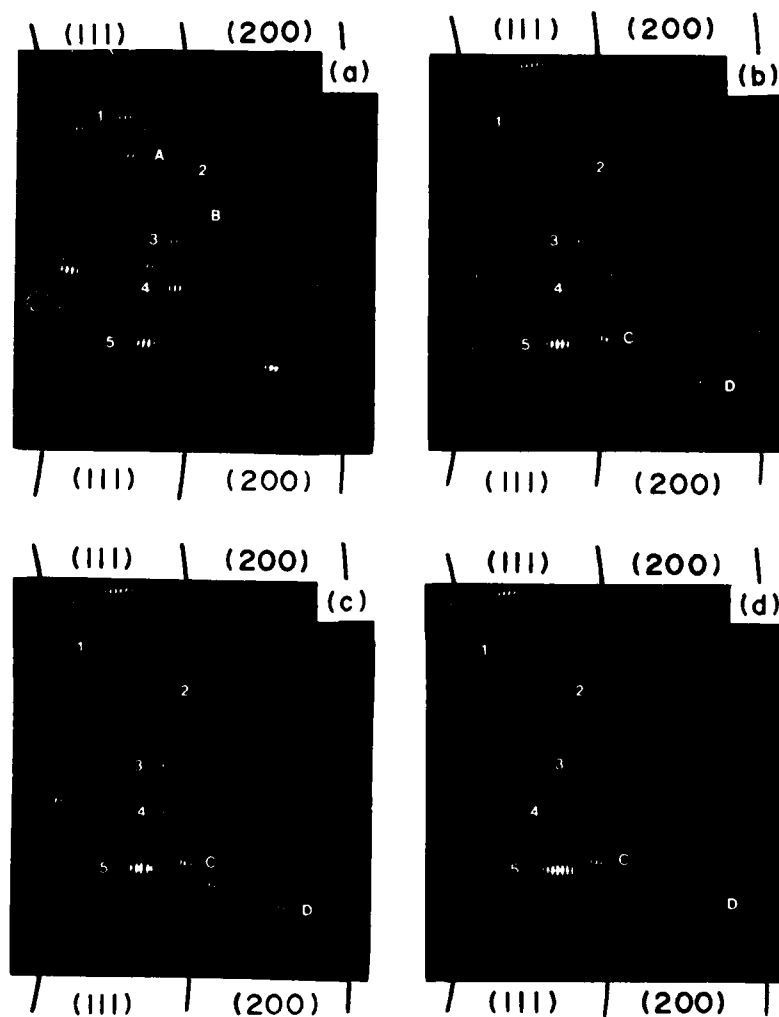


Figure 3. Dependence of Rocking Curves of Surface Grains on Applied Stress for Al-2024-T4 (Batch B). (a) Undeformed, (b) 138 MPa, (c) 207 MPa and (d) 276 MPa, $\text{CrK}\alpha_1$ radiation; Specimen Rotation = 2 minutes of arc.

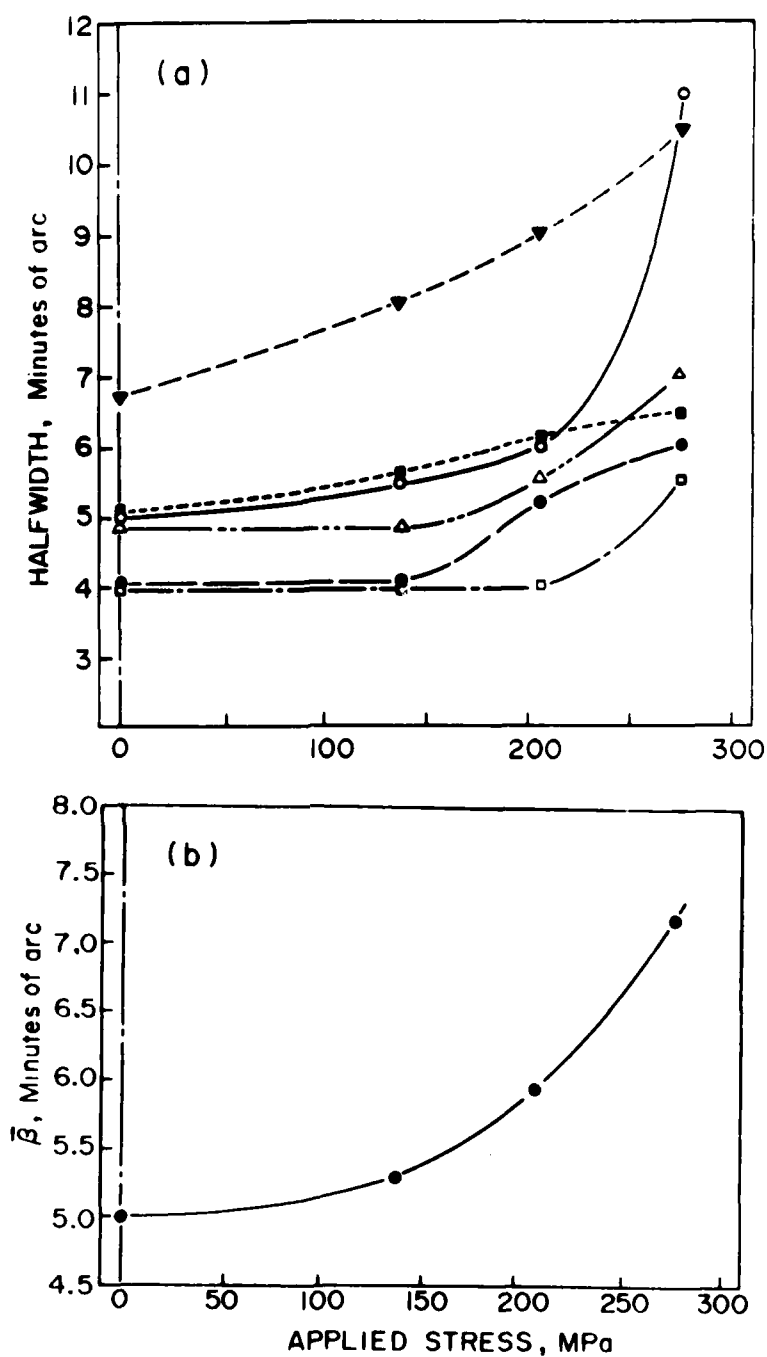


Figure 4. Dependence of Halfwidth on Applied Stress for Al-2024-T4 (Batch B).
 (a) Change in Halfwidth of Identical Reflecting Grains
 (b) Change in Average Halfwidth, $\bar{\beta}$

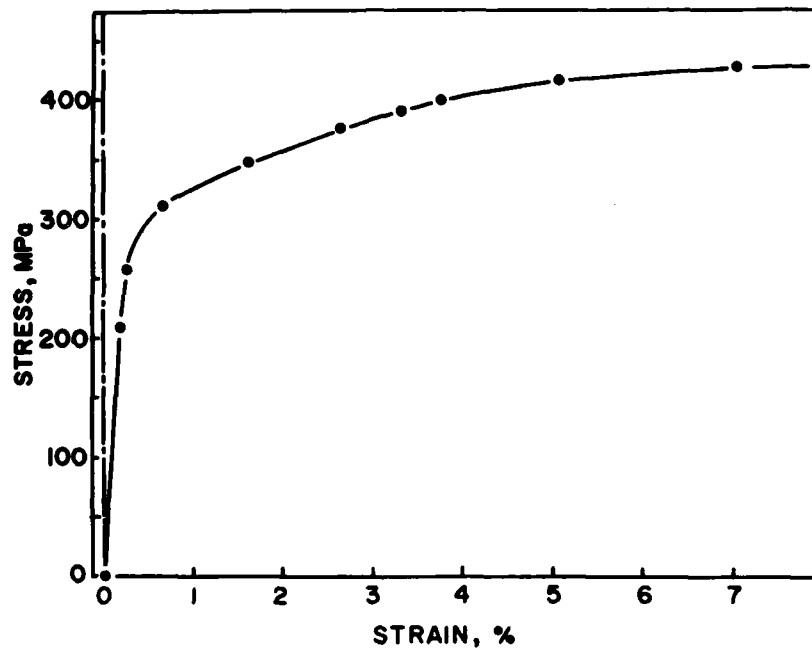


Figure 5. Stress-Strain Curve of Al-2024-T4 (Batch B).

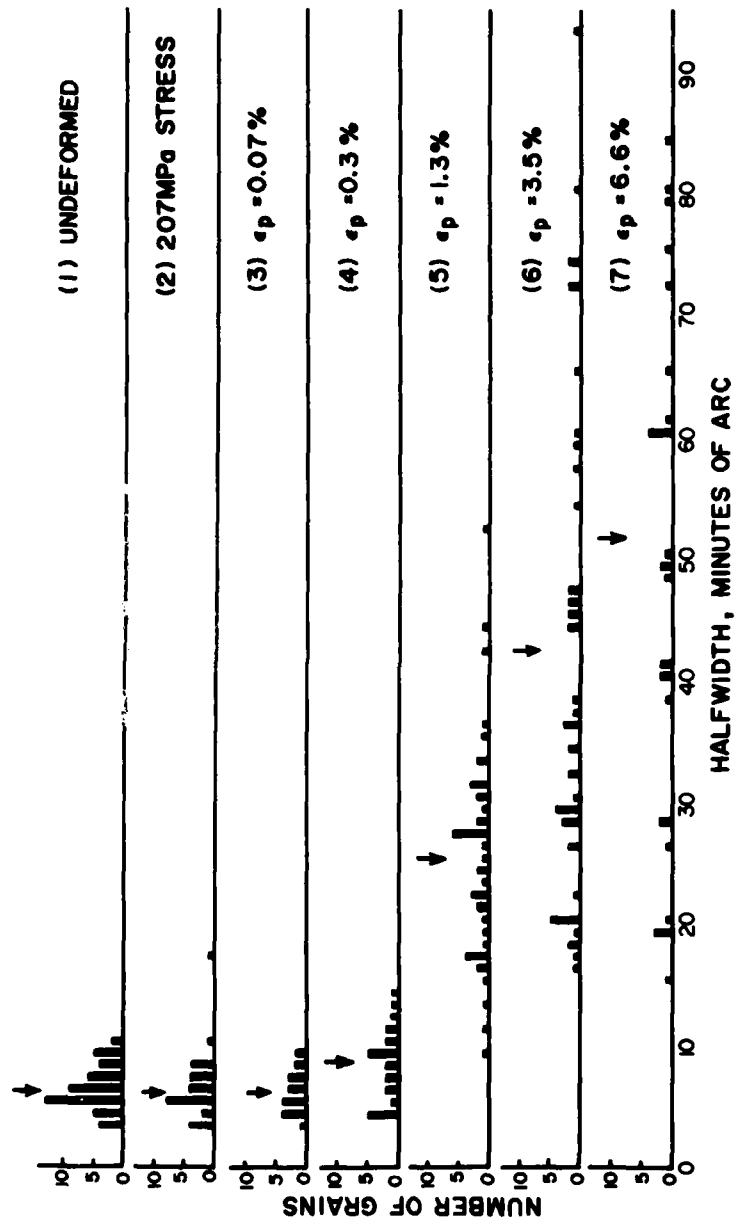


Figure 6. Distribution of Halfwidth as a Function of Applied Strain for A1-2024-T4 (Batch B). (Intensity Threshold Value = 50.)

noticeable change in the β distribution occurred at $\epsilon_p \approx 0.3\%$. From then on the β values of all grains increased with strain up to $\epsilon_p \approx 3.5\%$. Beyond this strain value the distribution appeared to be unchanged. The average halfwidth, $\bar{\beta}$, was plotted against plastic strain in Figure 7 for different intensity threshold values corresponding to 50., 100. and 200. counts, respectively. It will be noted that the $\bar{\beta}$ value increased linearly with the plastic strain up to 3.5%, beyond which value it exhibited saturation. The intensity threshold value was chosen on the basis of the signal to noise ratio, S/N. Since chromium $K\alpha_1$ radiation was used for the irradiation of the aluminum alloy, the background intensity was very low and hence for the annealed condition the S/N ratio was substantially high. As, however, the applied strain increased, the reflecting grains gave rise to very weak reflecting intensities covering a wide range of angles, which resulted in an increase of the background intensity for each rotation increment of the specimen. The background intensities obtained for each strain level are given in Table 2. It can be seen that for the collecting time of 10 seconds the background intensity was only 0-4 counts for small applied strains, while for larger plastic strains it was considerably higher. It will be seen that when the intensity threshold value of 50. was used, the S/N ratio decreased significantly as the applied strain increased. It became evident from Figure 7 that it is important in deformation studies to select a high threshold value in order to obtain reliable and reproducible β values.

TABLE 2 - MINIMUM BACKGROUND INTENSITY FOR EACH STRAIN LEVEL (A1-2024-T4: BATCH B) DATA COLLECTING TIME: 10 SECONDS

STRAIN	INTENSITY
undeformed	0
$\epsilon_p = 0.3\%$	1
$\epsilon_p = 1.3\%$	4
$\epsilon_p = 2.3\%$	9
$\epsilon_p = 3.5\%$	23
$\epsilon_p = 4.6\%$	22
$\epsilon_p = 6.6\%$	26

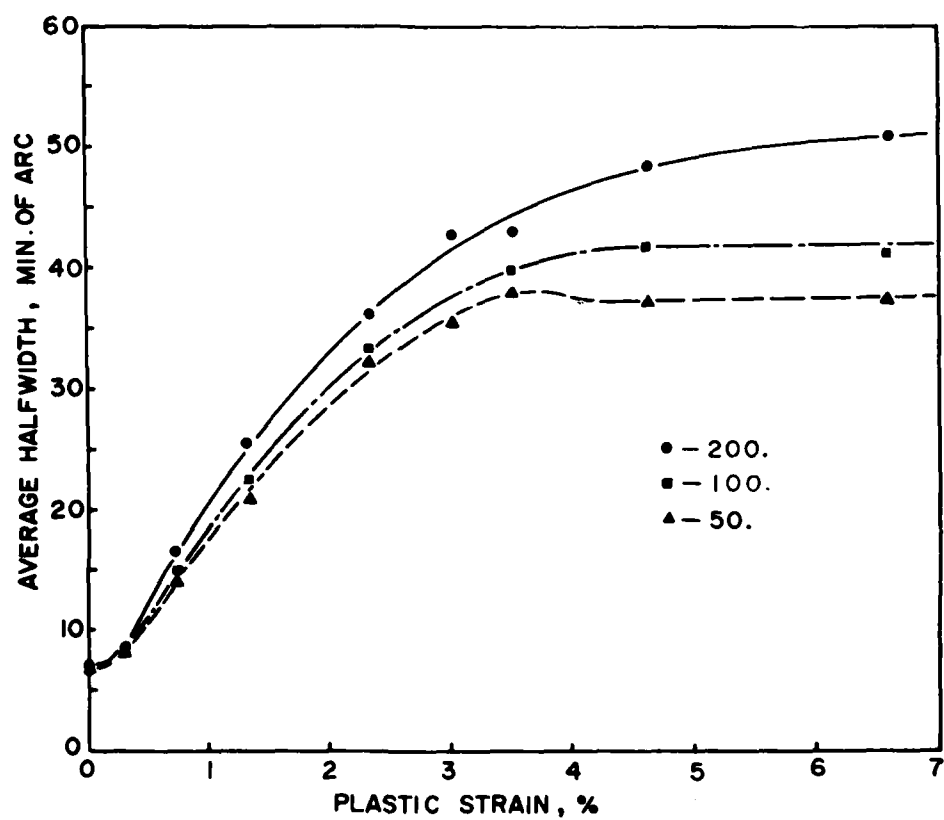


Figure 7. Effect of Intensity Threshold Value on Average Halfwidth at Various Plastic Strains.

B. Low-Cycle Corrosion Fatigue (LCCF) of Al-2024-T4 Alloy (Batch A) in 3.5% NaCl Solution

1. Comparison of Fatigue Behavior in Air and in 3.5% NaCl Solution

Fatigue cycling in air and in 3.5% NaCl solution was carried out. Figure 8 shows the S-N curves for $R=0.1$ in both environments. The endurance limit for air fatigue was observed to be about 220 MPa. The S-N curve obtained in 3.5% NaCl solution shows that the corrosion environment deteriorated the fatigue resistance at all stress levels and that the endurance limit observed in air was eliminated.

The rocking curve measurements were performed on specimens fatigued in both environments at 276 MPa maximum stress with $R=0.1$ at a frequency of 20 Hz. Figure 9 gives for the reflecting grains at the surface layer the dependence of the average halfwidth, $\bar{\beta}$, on the number of fatigue cycles. Both curves show very similar features: Initially the $\bar{\beta}$ value increased rapidly (Stage I), remained subsequently virtually constant (Stage II), and increased again (Stage III) when fatigue failure took place. It is of interest to note that the saturation of $\bar{\beta}$ values at Stage II observed in air was the same as that in the corrosive environment and that the only difference lies in the extension of Stage II; the extension in air being much longer than that in the 3.5% NaCl solution.

2. X-ray Analysis of Identical Grains Subjected to Low Cycle Corrosion Fatigue (LCCF)

The precise repositioning of a specimen before and after cycling made it possible to analyze the deformation behavior of identical grains of the aluminum alloy. Figure 10 exhibits X-ray rocking curves of reflecting grains for (111) and (200) reflections obtained at various fractions of the fatigue life. The specimen was fatigued at the maximum stress of 276 MPa with $R=0.1$ in 3.5% NaCl solution. The angular rotation increment of the specimen was 3 minutes of arc and $\text{CrK}\alpha_1$ radiation was used. Because of the low penetration capability of chromium radiation, the analysis was principally restricted to grains in the surface layer. It can be seen

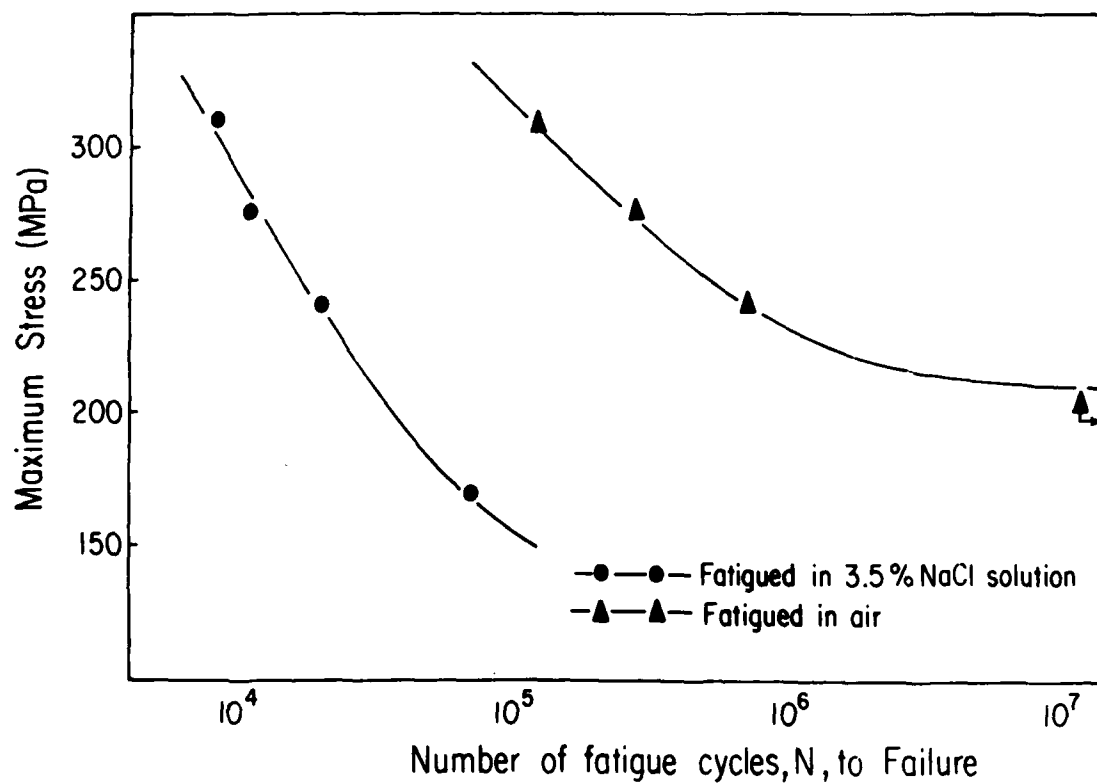


Figure 8. S-N Curve of Al-2024-T4 (Batch A) for $R=0.1$ in Air and 3.5 pct NaCl Solution. $f=20$ Hz.

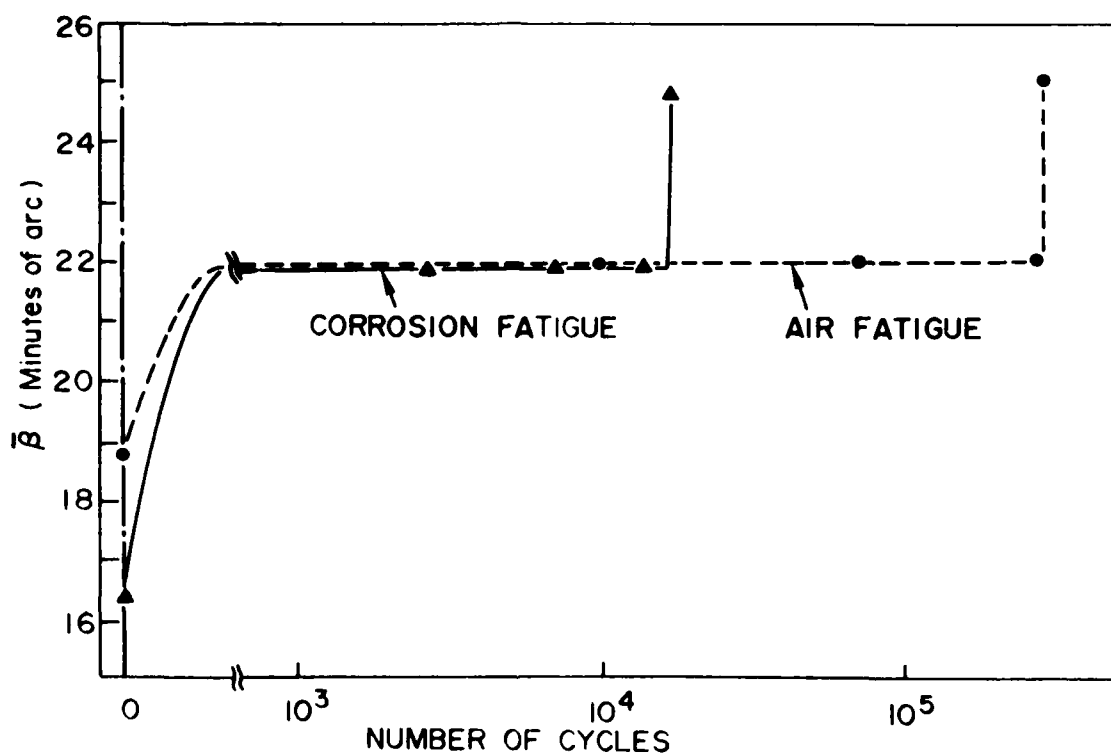


Figure 9. Dependence of Average Halfwidth, $\bar{\beta}$, of the Surface Grains on Number of Fatigue Cycles for Al-2024-T4 (Batch A) in Air and 3.5 pct NaCl Solution, $\sigma_{\max}=276$ MPa, $R=0.1$, $f=20$ Hz.

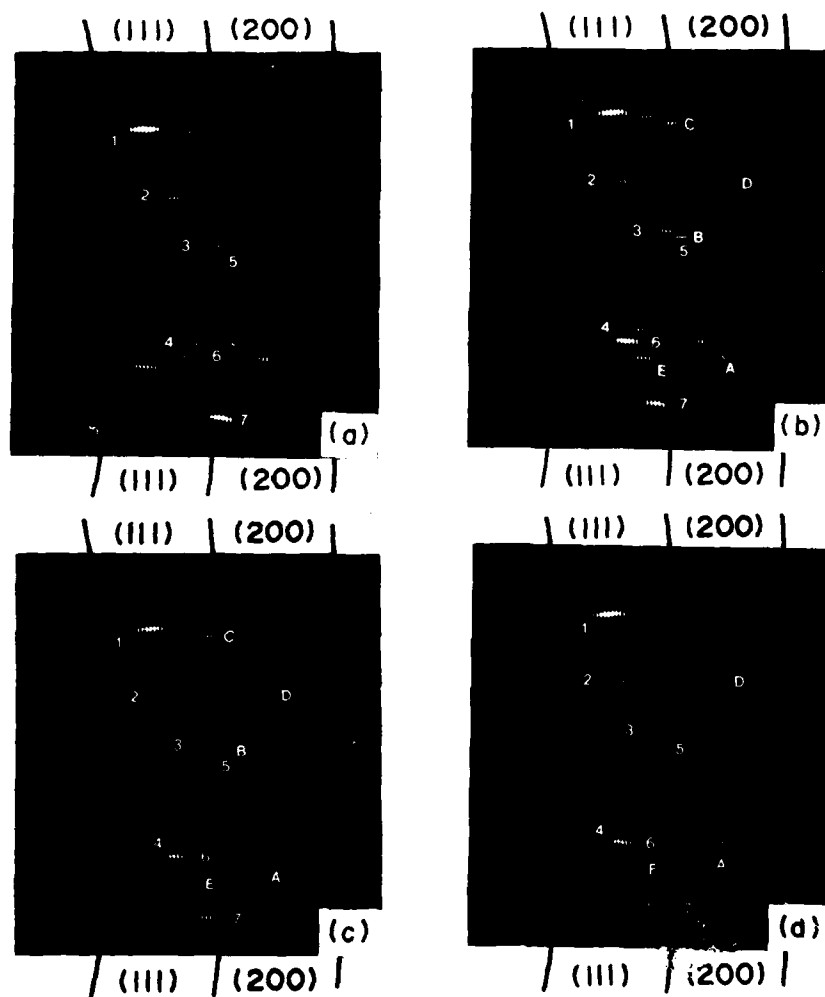


Figure 10. Dependence of Rocking Curves of Surface Grains on Corrosion Fatigue Cycles for Al-2024-T4 (Batch A) in 3.5 pct NaCl Solution at $\sigma_{max}=276$ MPa, $R=0.1$; (a) Undeformed, (b) 2,500 N (=22 pct N_F), (c) 8,000 N (=71 pct N_F) and (d) 11,100 N (=99 pct N_F), $CrK\alpha_1$ Radiation, Rotation Increment = 3 minutes of arc.

from Figure 10 that most of the grains, such as #1-7, retained their angular positions throughout the fatigue life. Some grains (#B and #C) came into reflecting position after the first cyclic increment, retained their angular reflecting range and then disappeared at failure, while other grains (#D and #E) retained their reflecting position even after failure. Figure 11(a) shows enlarged images of rocking curves of identical grains, taken from Figure 10, as a function of the fraction of fatigue life and Figure 11(b) represents their halfwidth dependence on fatigue life. It can be seen that almost all reflecting grains exhibited increases in halfwidth after Stage I cycling and remained virtually constant during Stage II cycling, until failure. At Stage III, some grains showed large increases in halfwidth, while others did not exhibit significant changes from those at Stage II.

3. Depth Distribution of Excess Dislocation Density Induced by Corrosion Fatigue

Specimens were fatigued in 3.5 NaCl pct solution at the maximum stress of 276 MPa with $R=0.1$ to 31, 67 and 99 pct of the fatigue life based on the S-N curve of Figure 8. The X-ray rocking curve measurements were carried out for each specimen as a function of the depth distance from the specimen surface; the results are shown in Figure 12. It may be seen that the $\bar{\rho}$ values at the surface layer were larger than those in the interior. The $\bar{\rho}$ values declined to a depth distance of about 50 μm from the surface and subsequently retained a plateau value throughout the interior of the specimen for each fraction of the life. However, unlike the specimens in air,⁸ the depth profile curves did not show a minimum and in this respect the shape resembled that of a monotonically deformed specimen.⁸ It should be noted that with cycling the $\bar{\rho}$ value at the surface layer approached rapidly saturation level, while that in the bulk, represented by the plateaus of the curves, increased more gradually with cycling. Furthermore, when fatigue failure set in the $\bar{\rho}$ value in the bulk reached practically the same value as that of the surface layer. It is this characteristic bulk response to cycling, showing relative to the surface grains a less rapid increase in $\bar{\rho}$, that leads to the determination of the accrued damage by the nondestructive X-ray method.

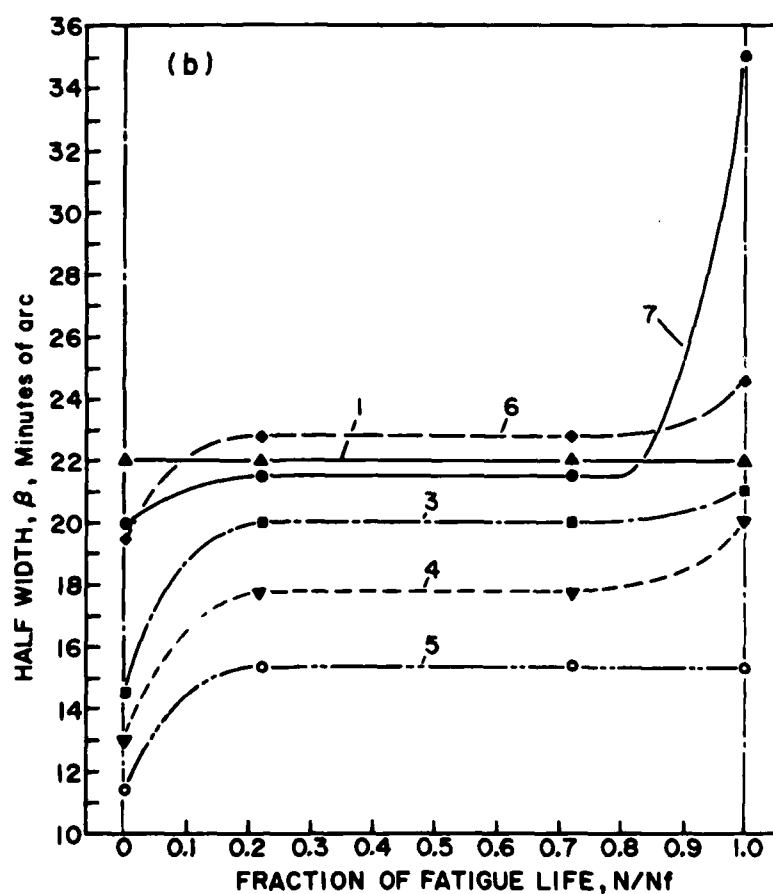
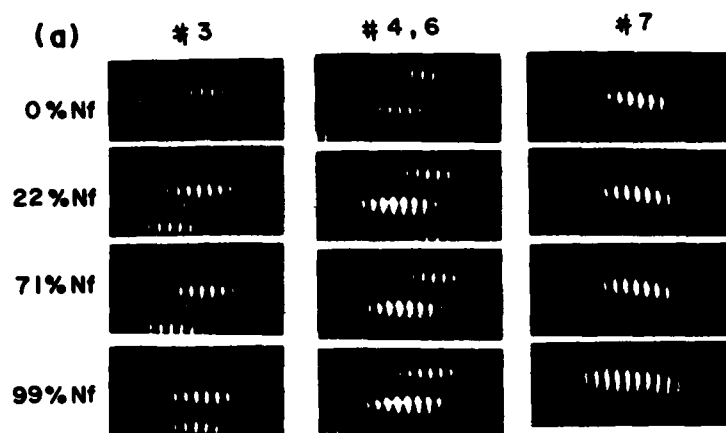


Figure 11. Dependence of Rocking Curve of Identical Grains on Corrosion Fatigue Cycles. Al-2024-T4 (Batch A), $\sigma_{\max} = 276$ MPa, $R=0.1$, 3.5 pct NaCl solution.
 (a) Details of Rocking Curves at Identical Grains
 (b) Halfwidth of Identical Grains

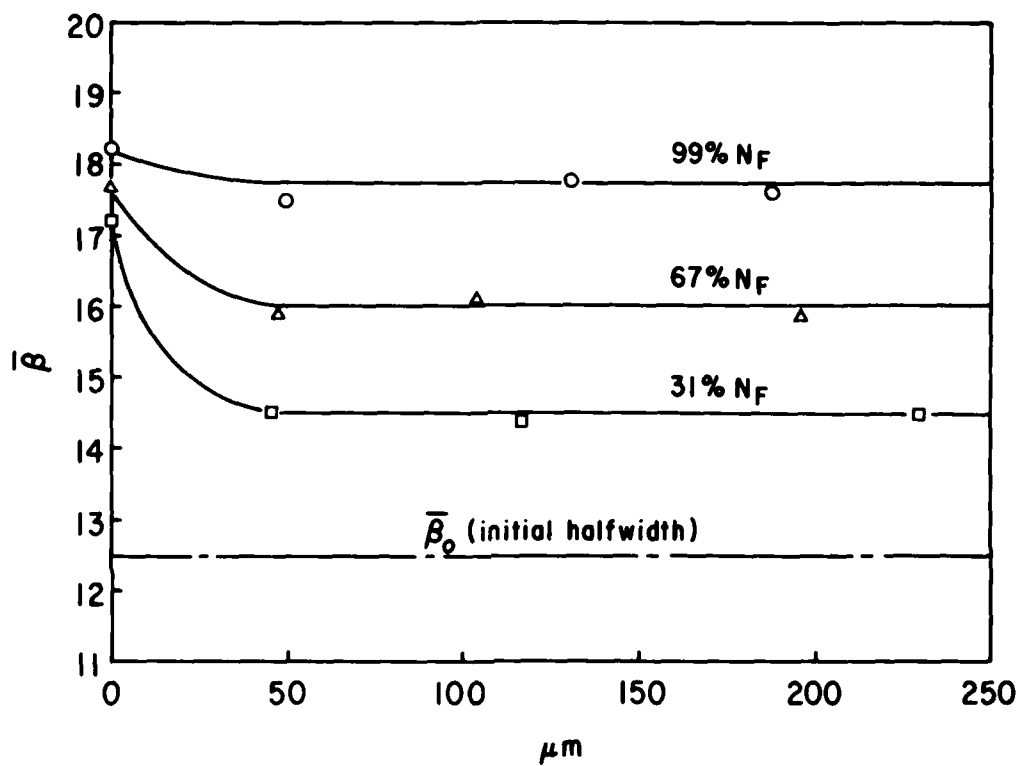


Figure 12. Dependence of Average Halfwidth, $\bar{\beta}$, on Depth Distance from Surface for Different Fractions of Corrosion Fatigue Life. Al-2024-T4 (Batch A), $\sigma_{max}=276$ MPa, $R=0.1$.

4. Determination of Accrued Damage and Failure Prediction by the Nondestructive X-ray Method

Figure 13 shows the dependence of the average rocking curve half-width, $\bar{\beta}$, on the number of fatigue cycles for various maximum stress levels with $R=0.1$. It will be seen that the stress levels were such that failure set in at a relatively low number of cycles and consequently the failure response falls into the category of LCCF. As indicated in this figure, the solid lines of the curves pertain to the measurements with $\text{CrK}\alpha_1$ radiation, while the dotted lines refer to those performed with $\text{MoK}\alpha_1$ radiation. It should be borne in mind that for chromium radiation, due to its long wavelength of 2.289 \AA , the absorption of the specimen is such that only surface grains can be analyzed. By contrast, the short wavelength of the molybdenum radiation ($\lambda=0.709 \text{ \AA}$) permits, also, analysis of the grains exceeding the $50 \text{ }\mu\text{m}$ depth distance from the surface. It will be seen from Figure 13 that for the maximum stress of 241 MPa with $R=0.1$ the $\bar{\beta}$ value increased during the first several hundred cycles. This increase was much more pronounced for the surface grains ($\text{CrK}\alpha_1$ radiation), which is in good agreement with the depth profile study of Figure 12. For subsequent cycling, the $\bar{\beta}$ value of the surface grains maintained virtually a plateau level until about 20,000 cycles were reached when a macroscopic crack propagation set in at point A, which corresponded to the critical halfwidth value, $\bar{\beta}^*$, of about 18 minutes of arc. By contrast, the $\bar{\beta}$ value of the bulk grains, obtained from $\text{MoK}\alpha_1$ radiation, exhibited a conspicuous ascent during cycling. It should be noted that the two curves pertaining to surface and bulk grains converged at point A.

For the maximum stress of 276 MPa with $R=0.1$, the two curves pertaining to surface and bulk grains were obtained. They show a perfect analogous behavior to that observed for the maximum stress of 241 MPa with $R=0.1$, namely, a sharp increase in $\bar{\beta}$ value early in the life, different slopes for bulk grains, and the convergence of the two curves at B, where catastrophic failure set in. The critical halfwidth, $\bar{\beta}^*$, obtained was about 18 minutes of arc. The increase of the maximum stress level from 241 to 276 MPa decreased the life by about half, from $N_F=20,000$ cycles to $N_F=11,100$ cycles. When with $R=0.1$ the maximum stress of 310 MPa was applied which was a higher stress than the static yield stress, the $\bar{\beta}$

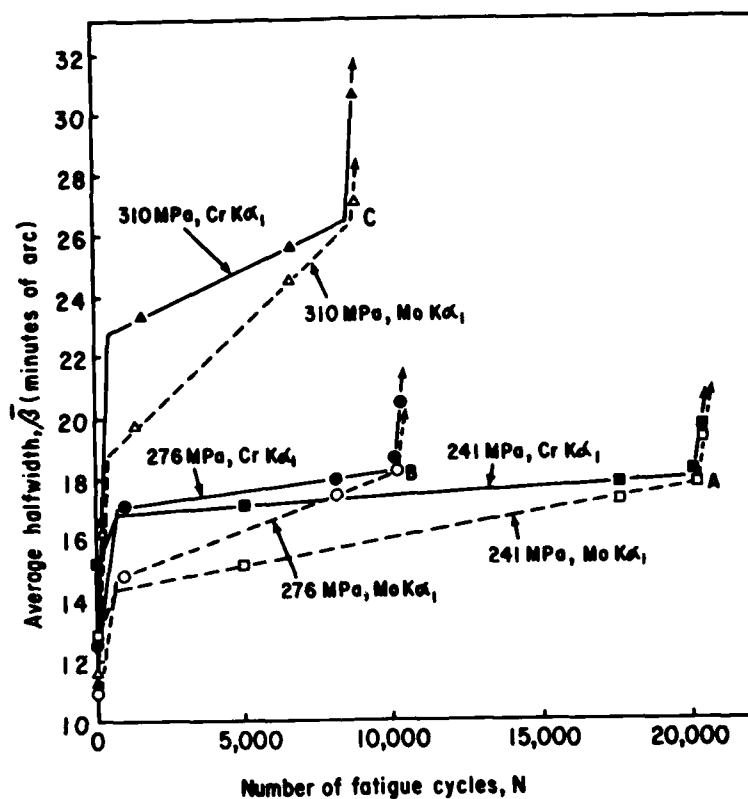


Figure 13. Average Halfwidth as a Function of Fatigue Cycles at Various Maximum Stresses, $R=0.1$, $f=20$ Hz (Batch A). Maximum Stress and X-ray Radiations are indicated.

value at the surface layer did not show any longer a plateau value but increased with cycling. The $\bar{\beta}$ value obtained from the bulk grain showed a similar behavior with a much steeper slope throughout the life. It should be noted, however, that the two curves converged again at C when propagation of a macrocrack set in. For this high stress level, the critical halfwidth value, $\bar{\beta}^*$, corresponding to the point C, was about 26 minutes of arc.

Figure 14 represents the ratios of the $\bar{\beta}$ value obtained from $\text{MoK}\alpha_1$ radiation to that obtained from $\text{CrK}\alpha_1$ radiation as a function of the fraction of fatigue life at various stress levels. A straight line relationship was obtained. When the branches pertaining to $\text{MoK}\alpha_1$ and $\text{CrK}\alpha_1$ converged, $\bar{\beta}_{\text{Mo}}/\bar{\beta}_{\text{Cr}}=1.00$ and the critical $\bar{\beta}^*$ was reached. At this value the excess dislocation density of the bulk was equal to that of the surface layer. On the basis of this criterion the accumulated damage induced by corrosion fatigue at any stage of the life as well as the fatigue failure could be predicted. When the specimens were cycled to failure at stress levels of 241, 276 and 310 MPa maximum stress with $R=0.1$, the predictions of corrosion fatigue failure, as may be seen from Figure 14, corresponded to 94, 95 and 98 pct of the actual lives, respectively.

The light micrographs of Figure 15 gave evidence and showed the importance of the criticality of $\bar{\beta}^*$. The micrograph of Figure 15(a) was taken at point A of Figure 13 when the specimen was corrosion-fatigued at 241 MPa maximum stress with $R=0.1$ to 20,000 cycles. Figure 15(b) corresponds to point B of Figure 13, when the specimen was cycled with 276 MPa. It will be seen that at this stage of life a major crack propagated catastrophically in the direction perpendicular to the loading axis (crack propagation Stage II).

Figure 16 may serve to demonstrate the capability of molybdenum $\text{K}\alpha_1$ radiation to penetrate owing to its short wavelength beyond the surface layer and thereby making the analysis of the defect structures in the bulk grains possible. The lower, steepest curve was constructed from the data points of Figure 12 and were collected from the plateau values of the bulk grains, as analyzed by chromium radiation, after electrochemical removal of the surface layer. The curve, pertaining to the $\text{MoK}\alpha_1$ radiation, on the other hand, was obtained with the workhardened surface layer intact. It is evident that the less steeper slope of the latter curve was due to

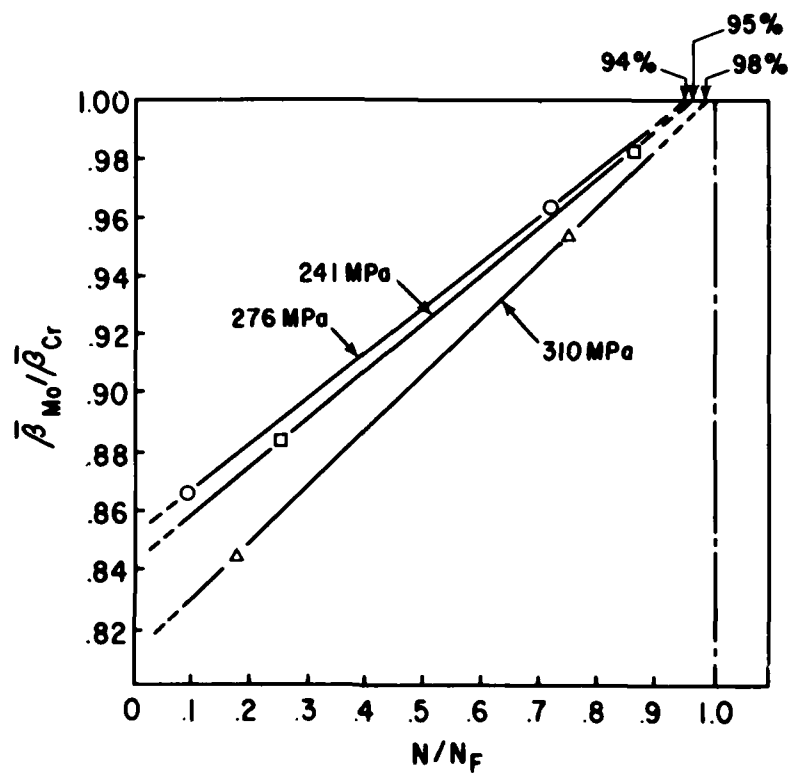


Figure 14. Ratios of $\bar{\beta}_{Mo}$ to $\bar{\beta}_{Cr}$ as a function of Fraction of Corrosion Fatigue Life at Various Maximum Stresses, $R=0.1$ (Batch A).

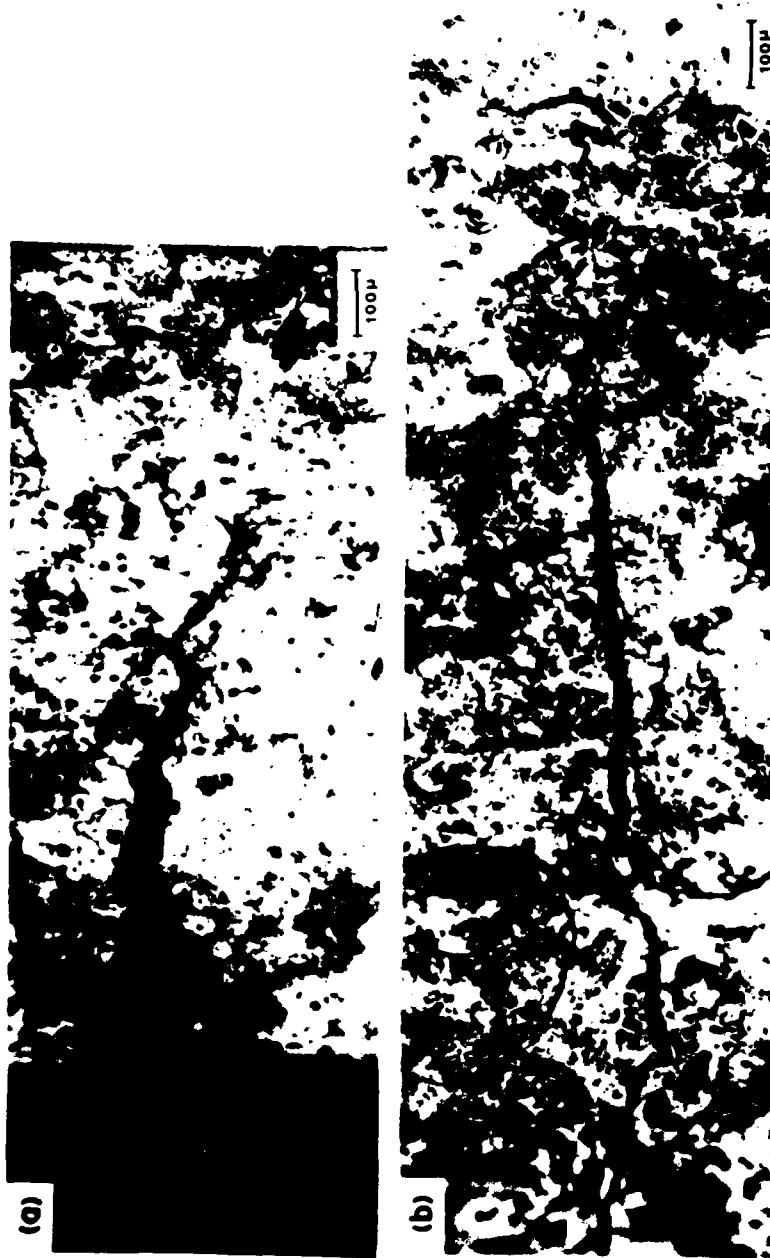


Figure 15. Light Micrographs Showing Propagating Cracks.

(a) After 20,000 cycles at $\sigma_{\max} = 241$ MPa, $R=0.1$, corresponding to Point A in Figure 13.

(b) After 11,100 cycles at $\sigma_{\max} = 276$ MPa, $R=0.1$, corresponding to Point B in Figure 13.

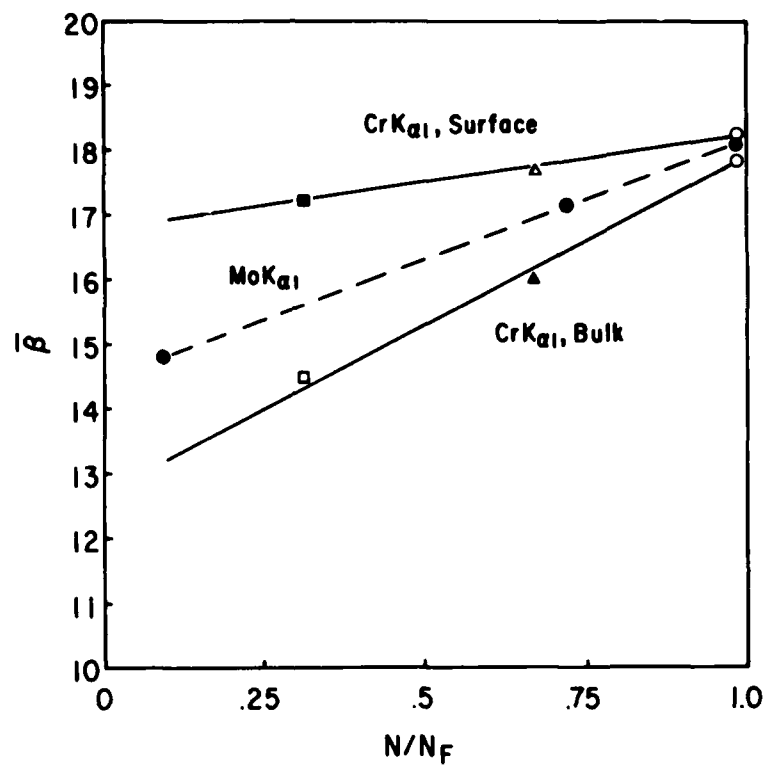


Figure 16. Surface and Bulk Dependence of Average Halfwidth on Fraction of Corrosion Fatigue Life. Al-2024-T4 Alloy (Batch A), $\sigma_{\max}=276$ MPa, $R=0.1$.

the fact that in the analysis employing molybdenum radiation some work-hardened surface grains were unavoidably also included. Nevertheless, the resulting slope was sufficiently steep to determine the critical $\bar{\beta}^*$ unequivocally. This curve can thus be used as a calibration standard to gauge the accrued damage at any stage of the corrosion fatigue life. If, however, both chromium and molybdenum radiation are employed at different fractions of the specimen's life, the ratio of the β values, as shown in Figure 14, will lead by extrapolation directly to $\bar{\beta}^*$ and thus to the assessment of the accrued fatigue damage and to failure prediction.

C. High-Cycle Corrosion Fatigue (HCCF) of Al-2024-T4 Alloy in 3.5 pct NaCl Solution

1. Dependence of Corrosion Fatigue Life on Cyclic Stress

Figure 17(a) and 17(b) show the S-N curve for $R=0.1$ and the R-N curve for $\sigma_{\max}=276$ MPa, respectively. Despite the fact that the maximum stresses were different, the two curves showed great similarities. Thus, as the cyclic stress decreased with decreasing mean stress as in Figure 17(a) or with increasing mean stress as in Figure 17(b), the fatigue life increased. A Goodman's diagram was constructed in Figure 17(c). The cyclic stress and the mean stress were calculated by the following relations:

$$\sigma_{\text{cyc}} = \frac{1}{2} \sigma_{\max}(1-R), \quad \sigma_{\text{mean}} = \frac{1}{2} \sigma_{\max}(1+R).$$

As shown in Figure 17(c) the fatigue strength in corrosive medium, defined in the present case as the cyclic stress below which no failure occurred after 5×10^6 cycles, was found to be about 40 MPa. Inspection of Figure 17(c) shows that the corrosion fatigue life depended strongly on the cyclic stress and not on the mean stress. For example, specimens which were fatigued at $\sigma_{\text{cyc}}=41$ MPa with $\sigma_{\text{mean}}=97$ MPa and 235 MPa, respectively, failed equally after about 1×10^6 cycles. To establish a basis of comparison between corrosion fatigue failure and stress corrosion behavior a static loading test in 3.5 pct NaCl solution was performed. Although a stress 350 MPa was applied in this test which was higher than the yield stress

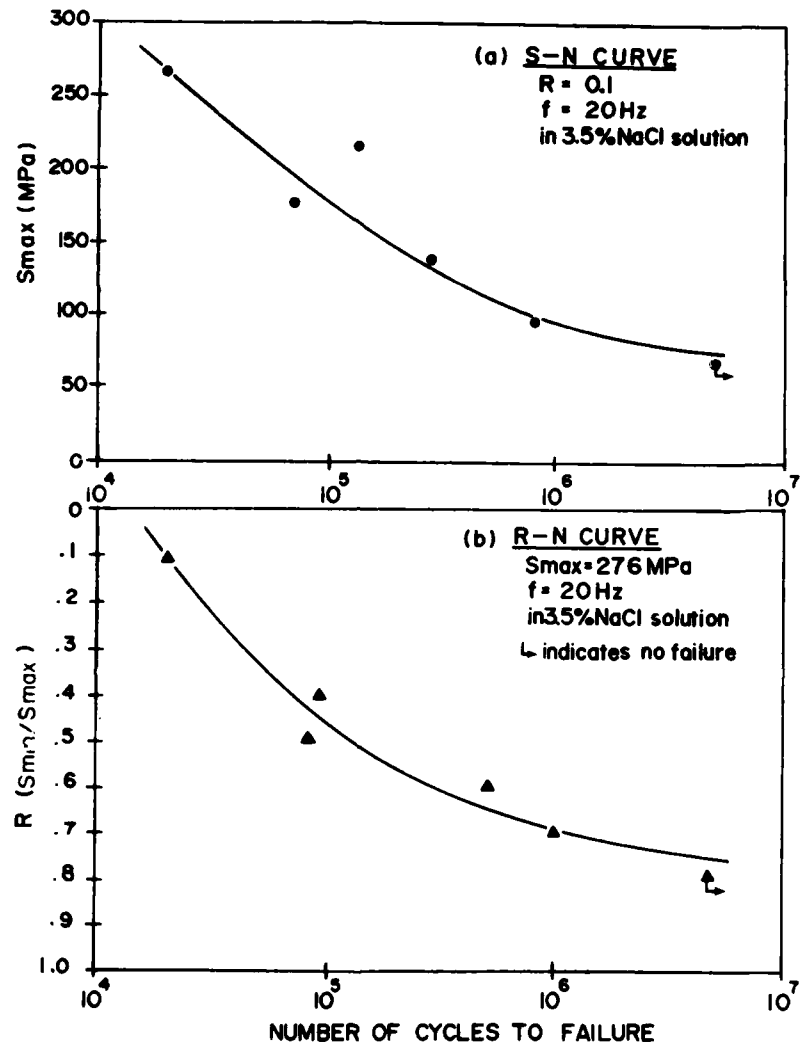


Figure 17. Al-2024-T4 (Batch B) in 3.5 pct NaCl Solution, $f=20 \text{ Hz}$.

(a) S-N Curve, $R=0.1$

(b) R-N Curve, $\sigma_{\max} = 276 \text{ MPa}$.

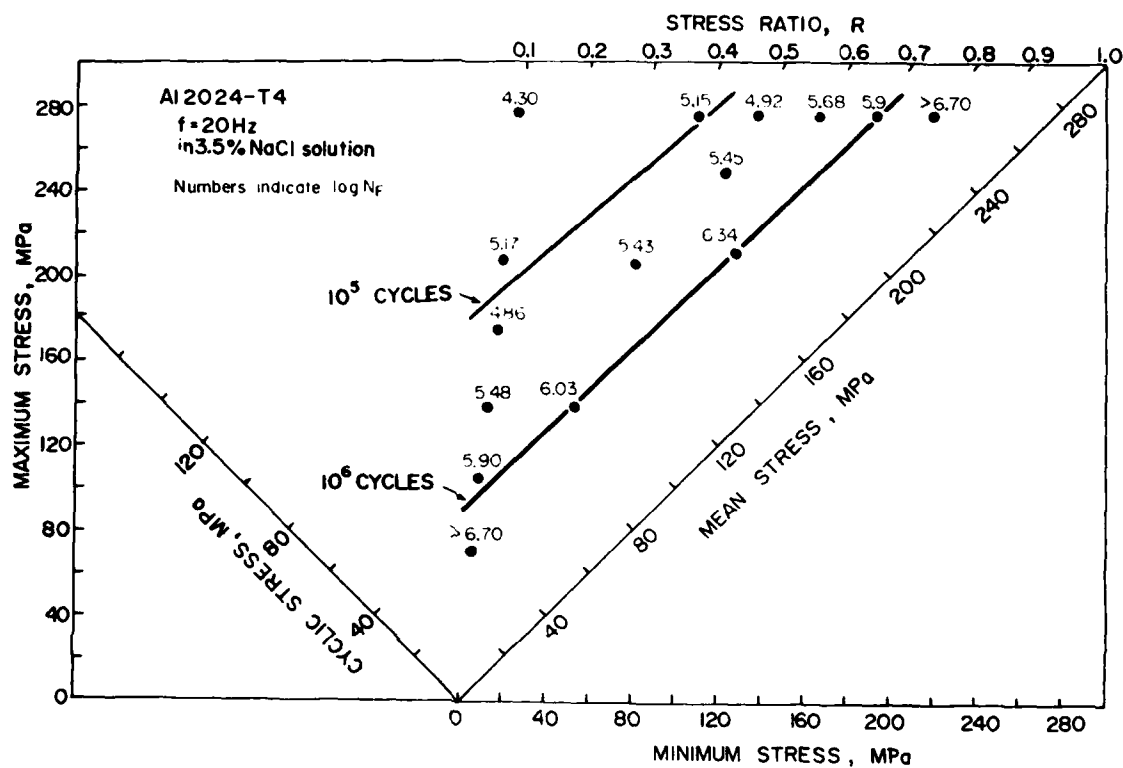


Figure 17(c). Goodman's Diagram of Al-2024-T4 (Batch B) in 3.5 pct NaCl Solution, $f=20 \text{ Hz}$.

(σ_y -276 MPa), no failure took place after 150 hours.

TABLE 3 - DEPENDENCE OF $\bar{\beta}^*$ ON APPLIED STRESS LEVELS

σ_{\max}	R	$\bar{\beta}^*(\min)$	σ_{cyc}	σ_{mean}
276 MPa	0.1	10.44	124 MPa	152 MPa
207 MPa	0.1	7.47	93	114
138 MPa	0.1	5.86	62	76
104 MPa	0.1	6.37	47	57
276 MPa	0.4	10.71	83	193
207 MPa	0.4	6.78	62	145
138 MPa	0.4	6.12	41	97
276 MPa	0.6	10.39	55	221
207 MPa	0.6	7.54	41	166
Annealed		6.01	0	0

2. Dependence of $\bar{\beta}^*$ on Maximum Stress

In the quest to assess the accrued fatigue damage in HCCF on the basis of the X-ray measurements and to correlate these measurements to the data of the Goodman's diagram in Figure 17(c), the CARCA method was employed. The $\bar{\beta}^*$ values of large grain populations were analyzed as a function of applied stress levels and R values. The resulting $\bar{\beta}$ distributions are shown in Figure 18. Inspection of this figure shows that the increases of the $\bar{\beta}$ values were principally controlled by the applied maximum cyclic stress and not by the mean cyclic stress. The critical $\bar{\beta}^*$ values at which catastrophic failure occurred were also analyzed by the CARCA method. The measurements were carried out after failure occurred and the fractured specimen was mounted carefully in the Y-Z Vernier of the DCD camera in such a way that the crystal monochromated $K\alpha_1$ radiation impinged on the area where crack formation had actually taken place. The $\bar{\beta}^*$ values thus obtained as a function of applied stress levels and R values are summarized in Table 3. It may be seen that in corrosion fatigue the induced microplasticity, expressed in terms of the $\bar{\beta}^*$ values, was principally

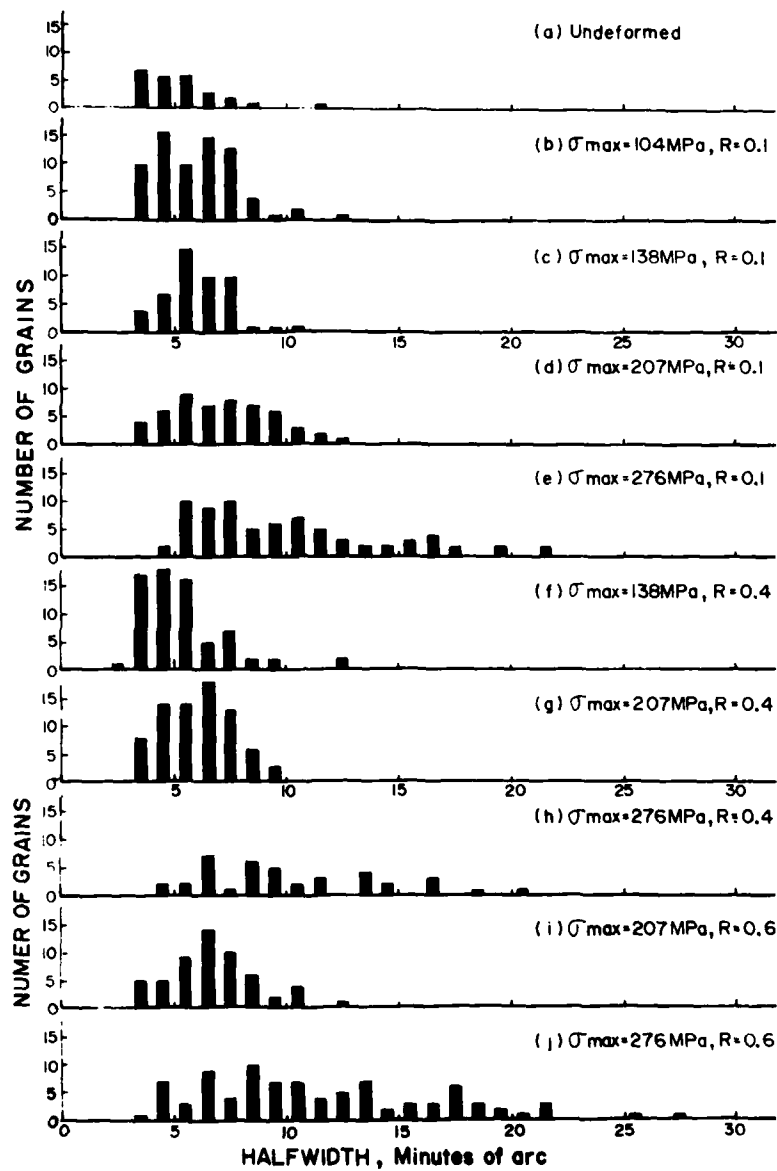


Figure 18. Distribution of Halfwidth at Various Stress Levels and R Values for Corrosion Fatigued Al-2024-T4 (Batch B).

controlled by the maximum applied stress. This $\bar{\beta}^*$ dependence is shown graphically in Figure 19. It will be noted that $\bar{\beta}^*$ did not increase appreciably until the maximum stress was higher than 160 MPa. This value corresponds to about 60 pct of the static yield stress. When higher stresses were applied $\bar{\beta}^*$ increased markedly and reached at the maximum stress level, corresponding to the yield stress, a value which was twice that of the undeformed specimen ($\sim 2 \bar{\beta}_0$). To assess the degree of microplasticity induced by corrosion fatigue, it is worth noting that when a monotonic stress of 350 MPa was applied to the specimen in the same environment the specimen did not fail and the average rocking curve halfwidth of the grains, $\bar{\beta}$, was as high as 30 minutes of arc. Evidently cycling in the corrosive environment lead not only to failure but also to reduced microplasticity.

It is very important to note that failure can occur in HCCF at stress levels considerably below 160 MPa, as may be seen from Figure 17(c). Thus in HCCF failure may occur at stress levels at which the applied X-ray method could not show any detectable increases in microplasticity over the undeformed state. It is evident, therefore, that in HCCF, when low stresses are applied, the measurements of the average halfwidth values, $\bar{\beta}$, of the grain population will not lead to an assessment of the accrued damage, as was the case in LCCF. For the latter case it was shown that the induced, overall microplasticity is a measurable quantity that could be used as a valuable diagnostic criterion for failure prediction (Section II-B-4).

3. Fracture Morphology

Figures 20(a)-20(b) show scanning electron fractographs of crack initiation and propagation on fracture surfaces. The right hand portion of Figures 20(a) and (b) depict the enlargement of the initiation site whereas the left hand portion gives an overall view of crack initiation and propagation morphology. Figure 20(a) which refers to a specimen fatigued in air, exhibits a well defined Stage I followed by Stage II crack propagation. When specimens were fatigued, however, in 3.5 pct NaCl solution at relatively high cyclic stress levels, viz. $\sigma_{cyc} = 124$ MPa, the fractograph displayed a modified river pattern characteristic of Stage I crack

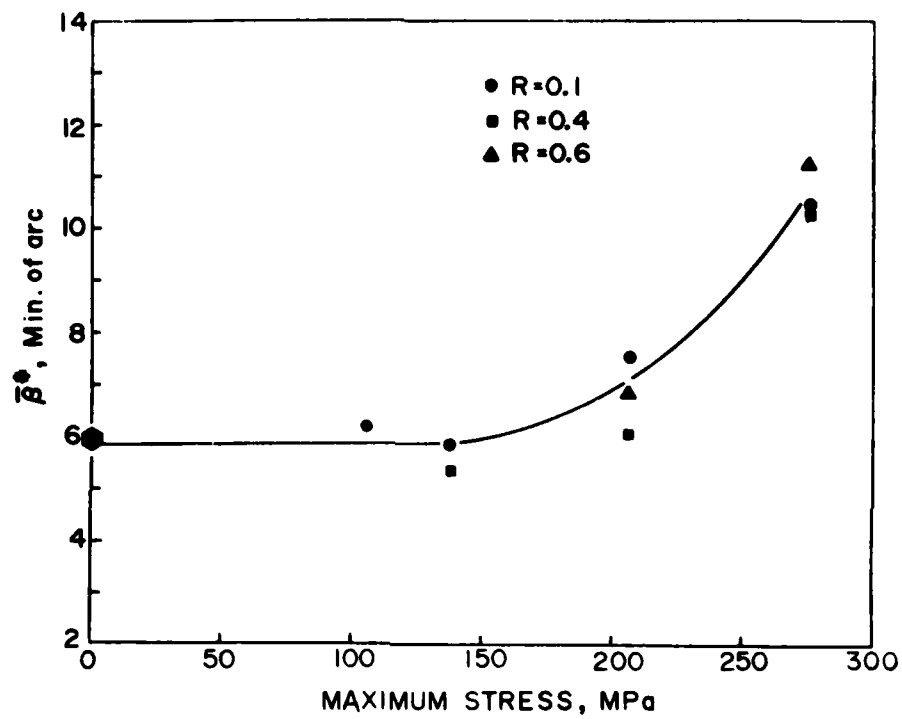


Figure 19. Dependence of Critical Halfwidth, $\bar{\beta}^*$, on Applied Maximum Stress for Corrosion Fatigued Al-2024-T4 (Batch B).

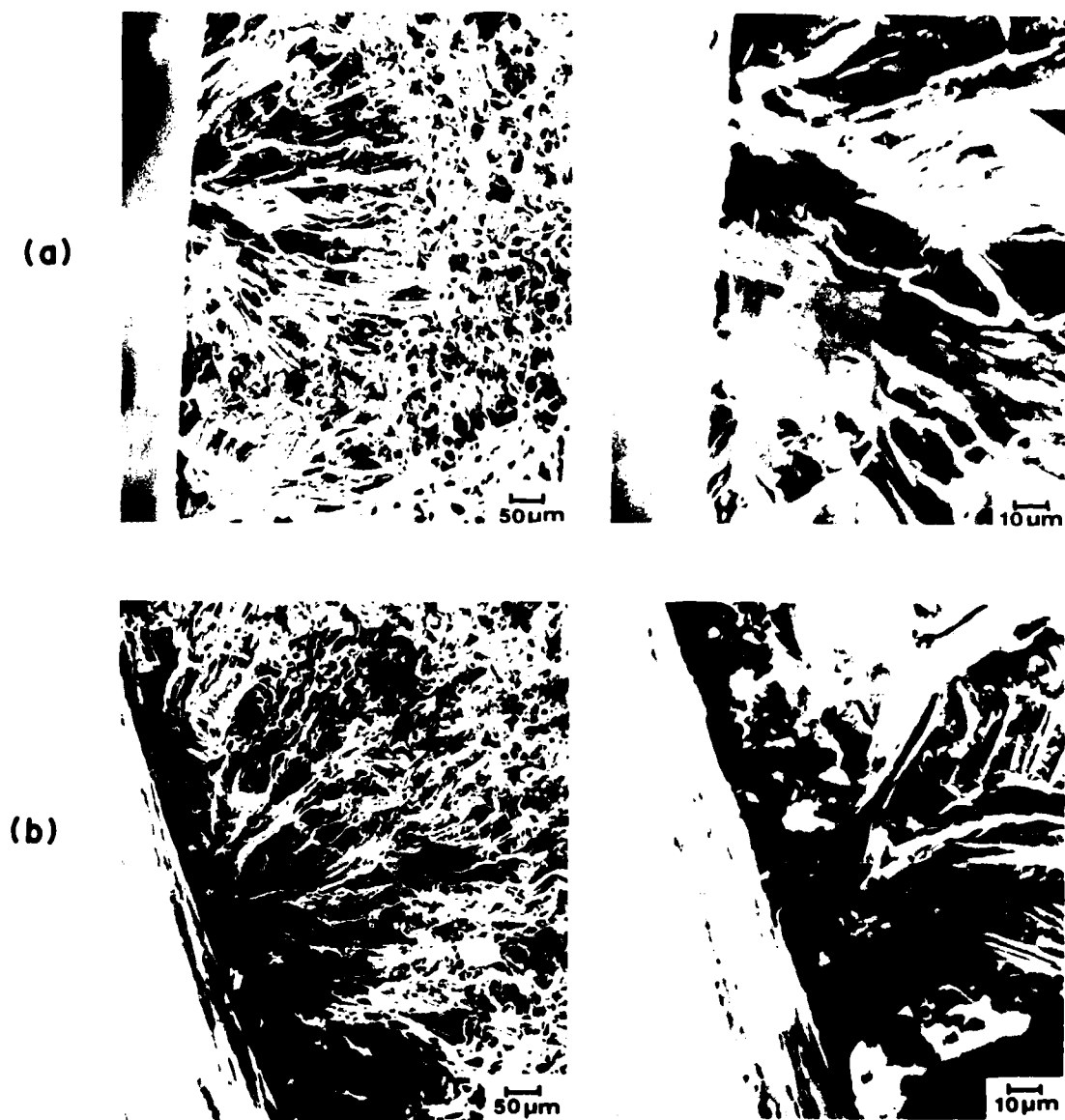


Figure 20. SEM Fractographs of Al-2024-T4 (Batch B), Cycled at
 $\sigma_{cyc}=124$ MPa, $\sigma_{mean}=152$ MPa, $f=20$ Hz.
 (a) Cycled in Air; $N_F \approx 311,500$ cycles
 (b) Cycled in 3.5 pct NaCl Solution; $N_F \approx 20,000$ cycles

propagation. It emanated from a single crack initiation site, as shown in Figure 20(b). Figure 20(c) shows the morphology of the crack opening stage (left side) and the morphology of the crack tip (right side). Figures 21(a)-21(c) exhibit the morphology of initiation sites of specimens fatigued in 3.5 pct NaCl solution with nearly the same cyclic stress ($\sigma_{cyc}=47$, 41 and 41 MPa) but varying mean stress ($\sigma_{mean}=57$, 97 and 235 MPa, respectively). As expected from the dependence of fatigue life on cyclic stress these three specimens had nearly the same life ($\sim 1 \times 10^6$ cycles). They exhibited also similar fractograph characteristics. Crack initiation was associated with a heavily corroded region which was surrounded by a featureless and quasi-cleavage-like area. From this area an ill-defined river line pattern characteristic of Stage I crack propagation extended well into the specimen. Figure 22 may serve to show the effect of reduction of frequency from 20 Hz to 0.5 Hz on the morphology of crack formation in corrosion fatigue. Because the maximum stress applied was 276 MPa at this frequency the strain rate of the cyclic deformation was virtually identical to that of Figures 21(a) to 21(c). Instead of a single crack initiation site the reduction in frequency resulted in profuse crack formation.

4. Effect of Applied Potentials on Corrosion Fatigue Life and Endurance Limit

Figure 23 shows the effect of applied potential on current flow of Al-2024-T4 alloy (Batch B) in 3.5 pct NaCl solution. The corrosion potential was measured at -880 mV. It may be seen that at the anodic potential side, the current flow increased linearly with applied potential. At the cathodic potential side, on the other hand, appreciable current flow did not occur up to -1500 mV.

It has been shown in Section II-B-1 that the fatigue resistance of the aluminum alloy of Batch A was considerably reduced in the corrosive medium (Figure 8). Batch B exhibits similar behavior; the fatigue limit was lowered from 280 MPa in air to 80 MPa in 3.5 pct NaCl solution. The application of an anodic potential lowered the fatigue limit even further. Figure 24 shows the S-N curves of the alloy (Batch B) for three different conditions. It can be seen that the S-N curve obtained under free corrosion potential was further suppressed



Figure 20(c). SEM Photographs of Crack Initiation Site (Left) and Crack Tip (Right) of Al-2024-T4 (Batch B) Cycled at $\sigma_{cyc}=124$ MPa, $\sigma_{mean}=152$ MPa, $f=20$ Hz in 3.5 pct NaCl Solution.

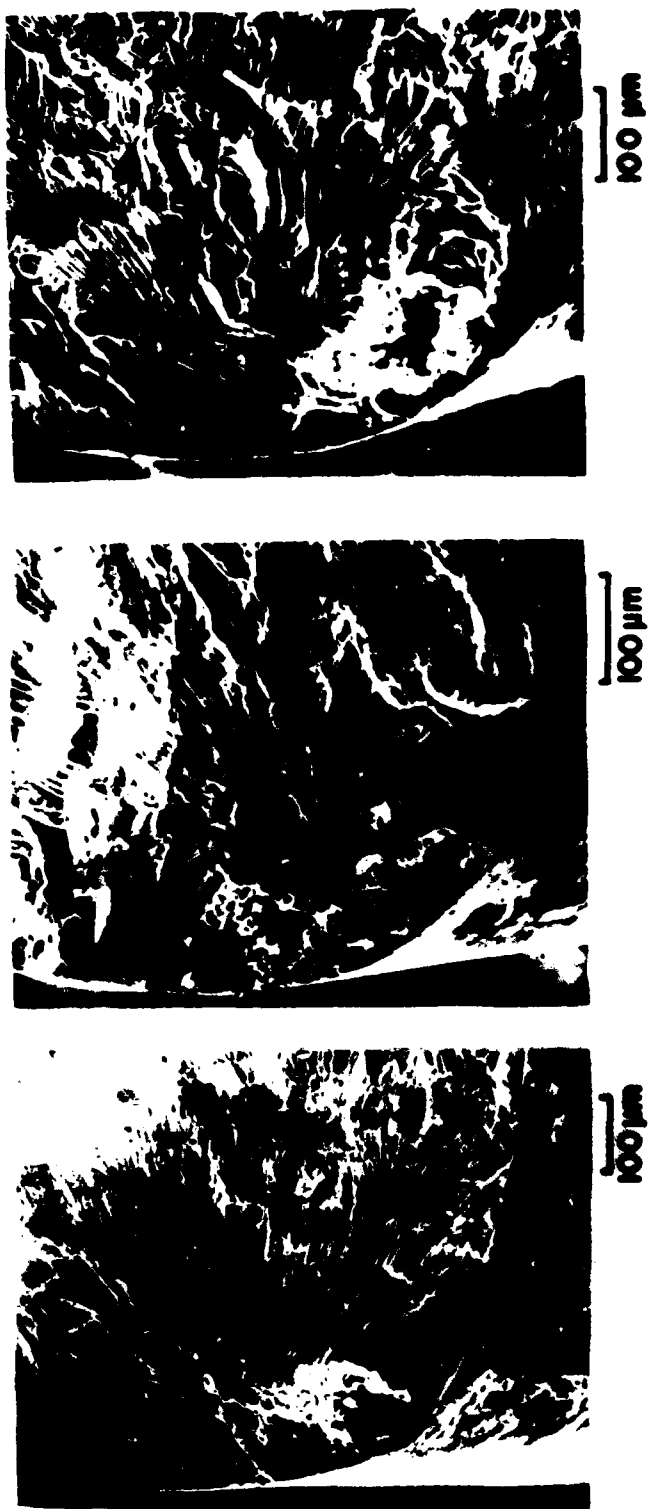


Figure 21. SEM Fractographs of Al-2024-T4 (Batch B) Cycled in 3.5 pct NaCl Solution at $f=20$ Hz.

- (a) $\sigma_{cyc}=47$ MPa, $\sigma_{mean}=57$ MPa; $N_F=900,000$ cycles
- (b) $\sigma_{cyc}=41$ MPa, $\sigma_{mean}=97$ MPa; $N_F=1,062,900$ cycles
- (c) $\sigma_{cyc}=41$ MPa, $\sigma_{mean}=235$ MPa; $N_F=969,800$ cycles



Figure 22. Effect of Frequency on Crack Formation of Al-2024-T4 (Batch B) Cycled at $\sigma_{cyc}=124$ MPa, $\sigma_{mean}=152$ MPa, $f=0.5$ Hz in 3.5 pct NaCl Solution.

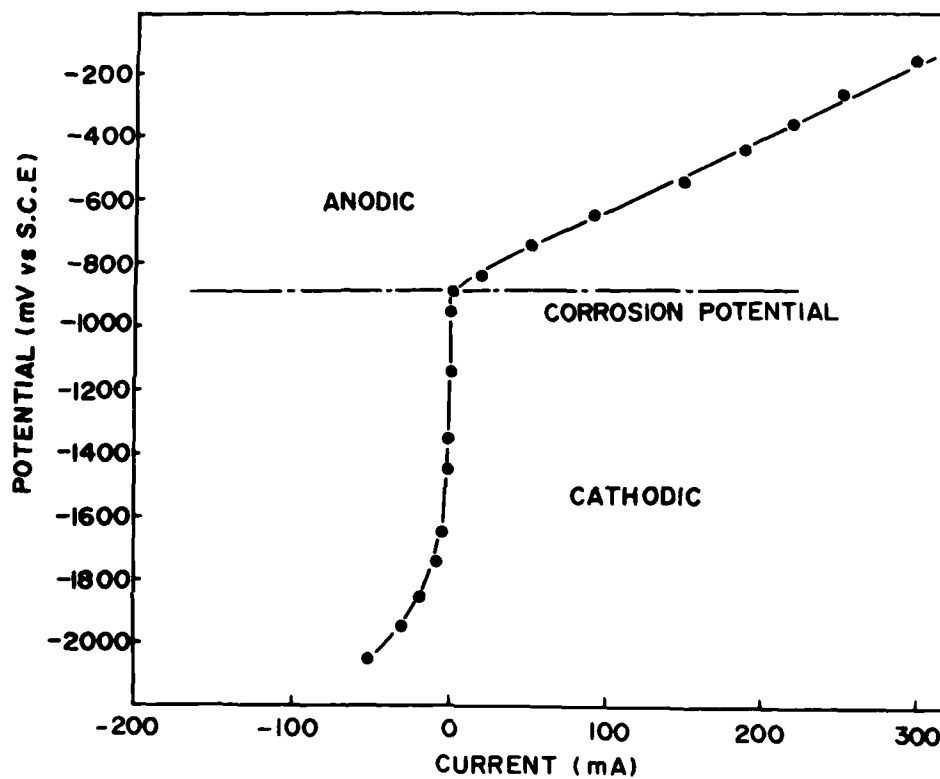


Figure 23. Effect of Applied Potential on Current Flow of Al-2024-T4 (Batch B) in 3.5 pct NaCl Solution.

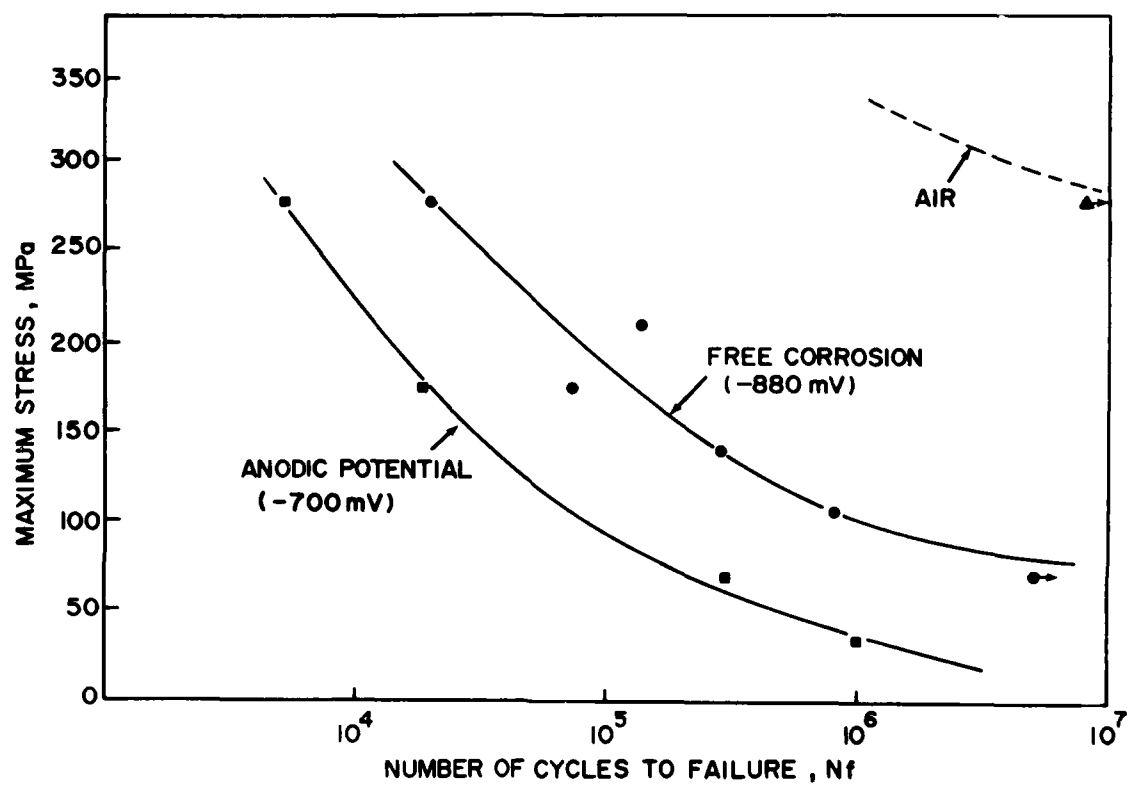


Figure 24. S-N Curves of Al-2024-T4 (Batch B) in Different Environments for $R=0.1$, $f=20$ Hz.

by an anodic potential of -700 mV toward the left and that the fatigue limit appeared to approach zero stress. The effect on fatigue resistance under free corrosion condition and applied anodic potential in 3.5 pct NaCl solution may be seen from the Goodman's diagram of Figure 25. It will be noted that the anodic potential (solid line curves) reduced the fatigue limit at all stress levels and that by applying the anodic potential the fatigue life became now dependent on both the cyclic stress and the mean stress (compare Figure 17(c)).

Figure 26 gives the dependence of the fatigue life on the R value for $\sigma_{\max} = 276$ MPa under four corrosion conditions, namely, free potential, anodic potential (-700 mV) and two cathodic potentials of -1500 mV and -1800 mV. It is of interest to note that there exist a linear relationship between the R values and the logarithm of the fatigue life under the influence of strong corrosion potentials, namely -700 mV and -1800 mV. Applying these potentials with $R=1.0$ the specimens failed without cyclic stress. Furthermore, compared to the free corrosion potential the R-N showed a large increase in fatigue life for small R values when a cathodic potential of -1500 mV was applied. For this potential, however, the fatigue life did not increase greatly with increase of the R value. For example at $R=0.8$ the specimen failed at -1500 mV after 3×10^6 cycles but did not fail after 5×10^6 cycles at the free corrosion potential. The effect of applied potential on fatigue life for different R values is shown in Figure 27. As shown previously, the fatigue resistance was greatly reduced at all stress levels when an anodic potential was applied. Application of cathodic potentials to the test specimens gave rise to characteristic nose-shaped curves with increases in fatigue life for smaller potentials and declines for larger potentials. For smaller R values (viz. $R=0.1$) the proportional increase in fatigue life was greater than for large R values (viz. $R=0.6$). It is of interest to note that the maximum in fatigue life for $R=0.1$ at -1500 mV (nose of the curve), shifted upward to about -1200 mV for $R=0.6$.

III. DISCUSSION

The studies, correlating microstructure to prefracture fatigue damage of Al-2024-T4, cycled in the corrosive medium of 3.5 pct NaCl solution, have clearly shown that a definite distinction should be made between the

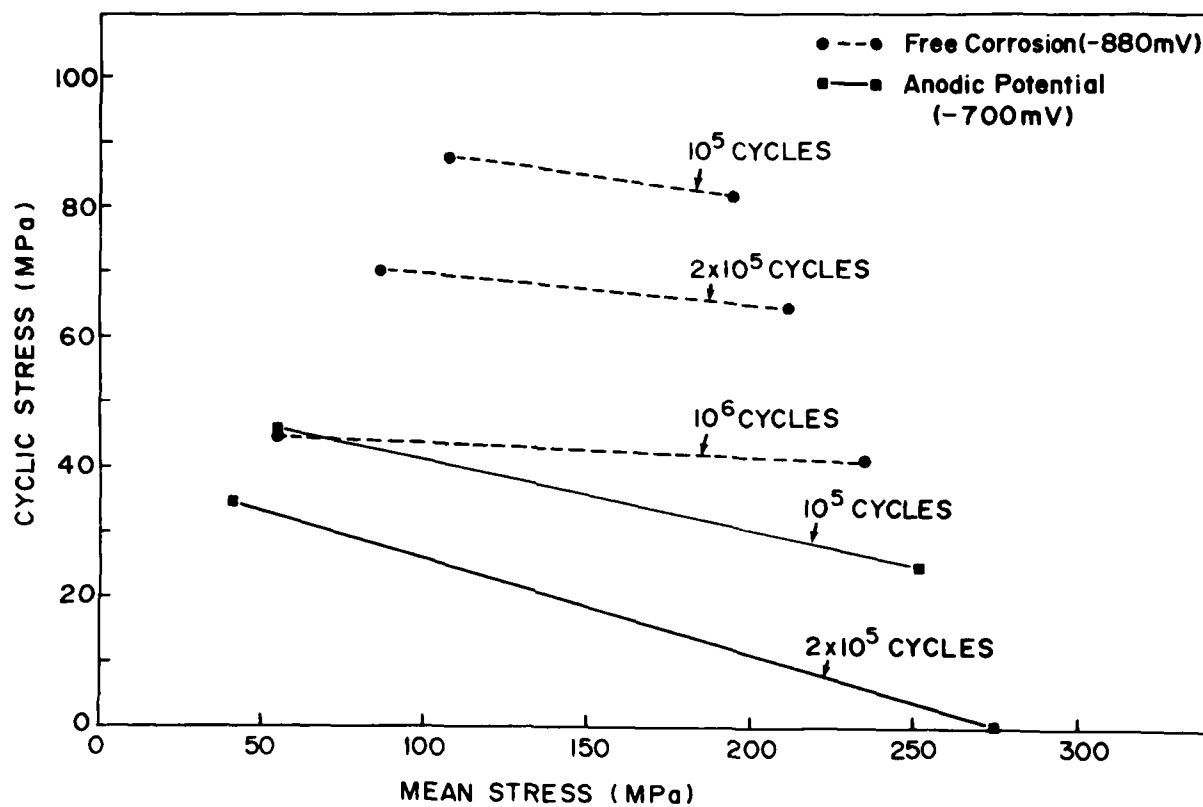


Figure 25. Goodman's Diagrams of A1-2024-T4 (Batch B) under Free Corrosion and Applied Anodic Potential in 3.5 pct NaCl Solution.

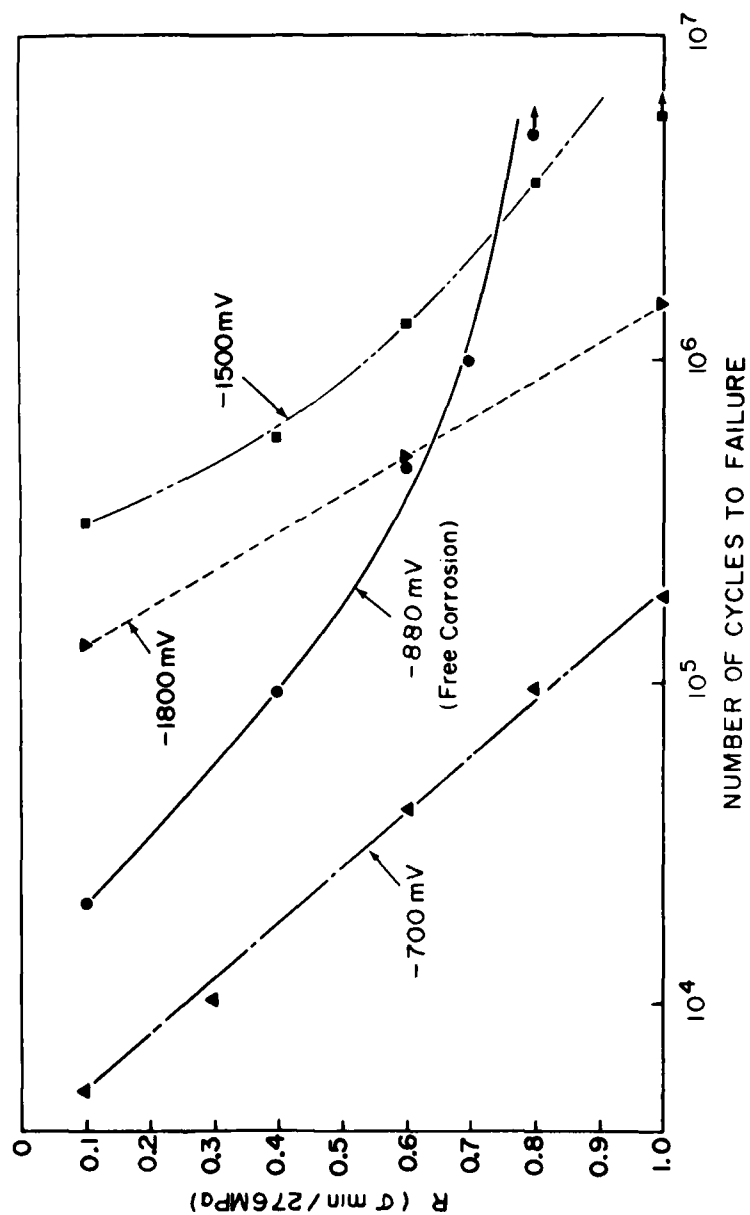


Figure 26. R-N Curves of Al-2024-T4 (Batch B) for $\sigma_{\max} = 276 \text{ MPa}$ under Various Corrosion Potentials in 3.5 pct NaCl Solution, $f = 20 \text{ Hz}$.

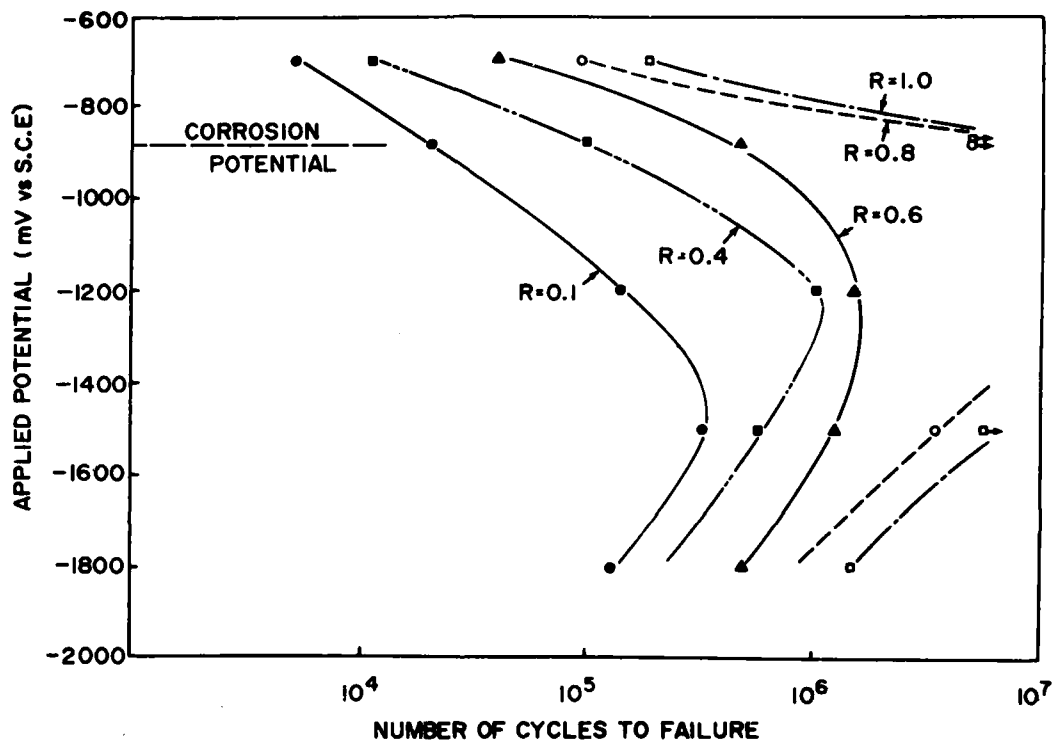


Figure 27. Effect of Applied Potential on Fatigue Life of Al-2024-T4 (Batch B) at Various R Values for $\sigma_{\max} = 276$ MPa in 3.5 pct NaCl Solution, $f = 20$ Hz.

alloy's response to low-cycle and high-cycle fatigue. In LCCF the high stress applied appears to be the major contributing factor in generating the dislocation arrangements and distributions which lead to fracture, while in HCCF the low stress applied has a much smaller effect and it is the chemical corrosion process and its local attack which appears to have predominance. For this reason these cyclic responses of the alloy will be discussed separately.

A. Low-Cycle Corrosion Fatigue

Because the applied cyclic stress in LCCF exerted a large influence on the generation, arrangement and distribution of dislocations, the cyclic response of Al-2024-T4 showed great similarities to that cycled in air. In analogy to the results obtained from the alloy cycled in air, this corrosion fatigue study has again demonstrated the interdependence in the development of the excess dislocation density of surface layer and bulk. The initial rapid rise of $\bar{\rho}$ of the surface grains in Stage I (Figures 12 and 13) is indicative of rapid workhardening of the surface layer with cycling. The maximum stresses applied were near the static yield stress and on cycling they activated dislocation sources at or near the surface more effectively than in the bulk. Since the surface grains did not exhibit on subsequent cycling a substantial increase in $\bar{\rho}$ during Stage II, the plateau branch of the curve in Figure 13 is attributed to the saturation of surface workhardening. It is interpreted to reflect physically the blocking effect of the surface layer which prevents the relaxation of excess dislocations accumulated in the bulk. By contrast, the initial rise of $\bar{\rho}$ of the bulk grains, which was much less than that of the surface grains, increased steadily during Stage II cycling (Figures 12 and 13), indicating that excess dislocations are being accumulated. When the excess dislocation density reached a critical value ρ^* such that the stress field associated with the accumulated dislocations exceeded the local fracture strength of the surface layer, catastrophic crack propagation took place (Figure 15). Experimentally, the determination of ρ^* corresponds to the determination of $\bar{\rho}^*$ and in accordance with the above concept $\bar{\rho}^*$ will lie on the point of intersection of the $\bar{\rho}$ curves of the surface and bulk grains. Thus, points A, B and C of Figure 13 reflect graphically the local, physical breakdown of the barrier effect of the surface layer for the respective,

applied stress levels. When the applied maximum stress was 310 MPa, hence considerably larger than the static yield stress, large plastic strains were accumulated by cycling. In this case it is interesting to note that not only was the ascent of the $\bar{\rho}^*$ value higher than the others, indeed approaching those obtained in air cycling,⁶⁻⁸ but the $\bar{\rho}$ curve of the surface grains did not exhibit a plateau region in Stage II. It will also be seen from Figure 13 that steeper $\bar{\rho}$ slopes for the bulk grains lead to a reduction in fatigue life. It should be kept in mind that in corrosion fatigue the cyclic stress effect and the chemical corrosive attack operate in tandem, affecting the development of prefracture damage in both Stage I and Stage II. Application of larger stresses shortens the life with the concomitant increases of the workhardening characteristics of surface and bulk grains. The corrosive attack is accelerated at dislocation sites and since the aqueous corrosive solution comes first in contact with the workhardened surface layer it will reduce its effectiveness in blocking pile-up dislocations, resulting in the reduction of fatigue life. It is because of the difference in the workhardening response of surface layer and bulk grains to cycling, that it was possible to assess experimentally the critical excess dislocation density ρ^* at which catastrophic crack propagation set in. This was accomplished by determining the incremental increase of workhardening in surface and bulk grains induced by cycling in terms of the $\bar{\rho}$ increases obtained from the X-ray rocking curve measurements. Radiation of different penetration depth was employed, $\text{CrK}\alpha_1$ for surface grain and $\text{MoK}\alpha_1$ essentially for bulk grain response, and in this manner it was possible to determine the prefracture damage and to predict failure by the nondestructive X-ray method (Section II-B-4).

B. High-Cycle Corrosion Fatigue

Corrosion fatigue resistance of aluminum alloys was studied by many investigators and it was found that the corrosive medium reduces the fatigue resistance and lowers and even eliminates the endurance limit obtained in air cycling.¹⁶ This investigation confirmed these results (Figure 8) and has demonstrated that the application of an anodic potential promoted the decline of fatigue resistance even more (Figure 24). These results are in agreement with those of other investigators.^{17,18,19} It was also shown

that when static loading was applied to the alloy immersed in the same corrosive medium as in cycling, no failure was observed even when the stress applied was higher than the static yield stress. In HCCF, however, crack initiation did take place and was associated with a corroded region from which a major crack developed (Figure 21). It is therefore evident that the cyclic stress is an essential ingredient for corrosion fatigue to occur.

The minimum cyclic stress required to cause failure was 40 MPa. The X-ray rocking curve measurements showed that the excess dislocation density did not increase above that of the undeformed specimen when the maximum stress was lower than 160 MPa (Figure 19). Consequently, the low stress level of 40 MPa did not induce a measurable overall microplasticity and the predominant contributing factor to HCCF appeared to be the local attack of chemical corrosion and not the applied stress. This effect of local corrosive attack became more pronounced when the frequency was lowered, resulting in severe pitting at inclusions and profuse crack formation (Figure 22). Reducing the frequency is comparable to reducing strain rate in the deformation process thereby extending the time element for corrosive attack.

Because of the conspicuous absence of an overall induced microplasticity in long-lived specimens when low stress levels were applied, and because of the time-dependence of the corrosion fatigue process, it is believed that a hydrogen embrittlement phenomenon is responsible for corrosion fatigue cracking. A similar conclusion was drawn by a number of investigators studying CF cracking in high strength aluminum alloys.²⁰⁻²⁵

At low cyclic stresses crack initiation and early propagation take up a large percentage of the fatigue life. Under such conditions hydrogen has ample time to diffuse to highly stressed regions, such as inclusion sites, and to promote the fatigue process.^{22,23} As pointed out by Jacko and Duquette²³ the effect of hydrogen on fatigue behavior of aluminum alloys does not depend strongly on bulk diffusion of hydrogen but only requires that hydrogen be present in the vicinity of the tip of a microcrack. This may be a local microplastic zone. In such a region fresh metal is constantly exposed to the corrosive environment. As suggested by Tien²⁶ and Johnson and Hirth²⁷ dislocations in the microplastic zone may act as promoters of high diffusivity paths for hydrogen and thus aid

in increasing the hydrogen concentration at the crack tip.

The results of this investigation obtained for the effect of applied potential are quite similar to those reported by Jacko and Duquette²³ and also by Endo et al.²⁸ As may be seen from Figure 27 initial cathodic polarization suppressed electrochemical corrosion which delayed crack initiation and propagation and resulted in increased fatigue lives. Additional cathodic polarization, however, resulted in increased crack initiation and reduction of lives which Endo et al. attributed to embrittlement resulting from excess hydrogen ions. It will be noted in Figure 27 that these polarization effects became particularly pronounced for small R values. It appears, therefore, that the rate determining process in aqueous fatigue of the aluminum alloys is the adsorption of hydrogen in either the alloy surface or in the plastic zone ahead of the crack tip. This process may be facilitated by chemical means such as Cl^- environment, pH or cathodic charging or mechanical deformation.²³ The rate determining step, however, may differ for different chemico-mechanical conditions. Thus, when the cyclic stress levels were increased and crack propagation rather than crack nucleation took up most of the time, as was the case in LCCF, the maximum applied stress became increasingly the rate determining step for failure. It was the dominating effect of the applied maximum cyclic stress with the concomitant increases in microplasticity that lead to the determination of the accrued fatigue damage and failure prediction in LCCF, discussed in Section III-A.

IV. SUMMARY

1. Cycling Al-2024-T4 in the corrosive medium of 3.5 pct NaCl solution reduced the fatigue resistance and lowered and even eliminated the endurance limit obtained in air. Application of an anodic potential promoted the decline of fatigue limit.
2. In high cycle corrosion fatigue (HCCF) fatigue life is not determined by the maximum applied stress but rather by the mean cyclic stress.
3. The absence of an overall induced microplasticity at very low applied cyclic stresses, viz. 40 MPa, the frequency dependence as well as the observed cathodic polarization effects suggest that in HCCF hydrogen embrittlement may be the rate determining process.

4. In low cycle corrosion fatigue (LCCF), when the largest percentage of life was taken up with crack propagation, the maximum applied stress became the rate determining step for fatigue failure.
5. In LCCF the grains at the surface workhardened much faster than those in the bulk. When the increase of the excess dislocation density, ρ , in the bulk reached the critical value ρ^* the local fracture strength of the surface layer was exceeded and catastrophic crack propagation took place.
6. Carrying out X-ray double crystal diffractometer measurements and determining the build-up of the excess dislocation density in surface and bulk, using X-ray radiation of different penetration depth, the accrued prefracture damage in LCCF was determined and the onset of catastrophic failure was predicted by the nondestructive method.

Part II: Determination of Fatigue Damage of Ti-6Al-4V Cycled in Air

I. EXPERIMENTAL PROCEDURE

Cylindrical specimens with two parallel flat surfaces, suitable for X-ray investigations, and gage length of 7.6 mm were annealed at 980°C for 1 hour in vacuum, followed by furnace cooling. The specimens were mechanically polished and subsequently electropolished at -30°C in a solution of 59 pct methanol, 35 pct n-butylalcohol and 6 pct perchloric acid. This solution was used for the removal of the surface layers of cycled specimens as well as for the preparation of thin foils for TEM investigation. Load controlled tension-compression fatigue tests were performed in air on an Instron hydraulic testing machine (model 1350) at 10 Hz.

In order to investigate the role of the surface layer, specimens were fatigued for various life fractions at a stress of 629 MPa and then fatigued to failure at stresses above as well as below the fatigue limit. Similarly, specimens were fatigued at these lower stresses after removing the surface layer formed during the fatiguing at 629 MPa.

For the characterization of the defect structure induced by fatigue, light metallography, X-ray diffraction, SEM and TEM investigations were

carried out. Employing an X-ray double crystal diffractometer (DCD) method, rocking curve halfwidth measurements of the individual grains in surface and subsurface layers were performed.^{12,13} Thin foils for TEM investigation were prepared with the aid of a twin jet electropolishing unit. Special precaution was taken to prepare foils of the cycled specimens with the surface layer intact. The specimen surface was given a protective coating and was then electro-polished from the other side of the coated surface. Subsequently, the protective coating was chemically dissolved. Foils were examined in a JEM 200A electron microscope at 200 KV.

II. RESULTS

A. Effect of Pre-Fatigue Damage and Removal of Surface Layer on Fatigue Life

Figure 28 shows the S-N curve of an annealed specimen. It will be seen that the fatigue limit is about 400 MPa. By contrast the S-N curve of a specimen which was pre-fatigued at a high stress, 629 MPa, to 90 pct of its life, no longer exhibited an endurance limit. When, however, a surface layer of about 100 μm was removed from a specimen subject to the same severe pre-fatigue conditions (90% N_F at 629 MPa) the S-N curve obtained exhibited a remarkable extension of life for every stress level. From Figure 28 it may be seen, however, that surface removal of such severely pre-fatigued specimen could not restore fully the fatigue behavior to that alloy without pre-fatigue treatment.

The data in Figure 29 give the dependence of pre-fatigue cycling on the subsequent S-N relationships. The curves marked by filled circles and triangles in Figure 29 refer to the specimens cycled at stresses of 472 and 315 MPa; these cyclic stresses correspond to 60 pct and 40 pct of the static yield stress, respectively. Figure 29 shows that for the cyclic stress of 472 MPa there exists a linear relationship between the logarithm of the number of cycles and the fraction of life at the pre-fatigue stress. For the cyclic stress of 315 MPa, which is a stress below the fatigue limit, the number of cycles to failure also shows a linear logarithmic dependence for values above about 25 pct of life expected at the 629 MPa stress level. When cycled for a period less than about 25 pct of the life expected at

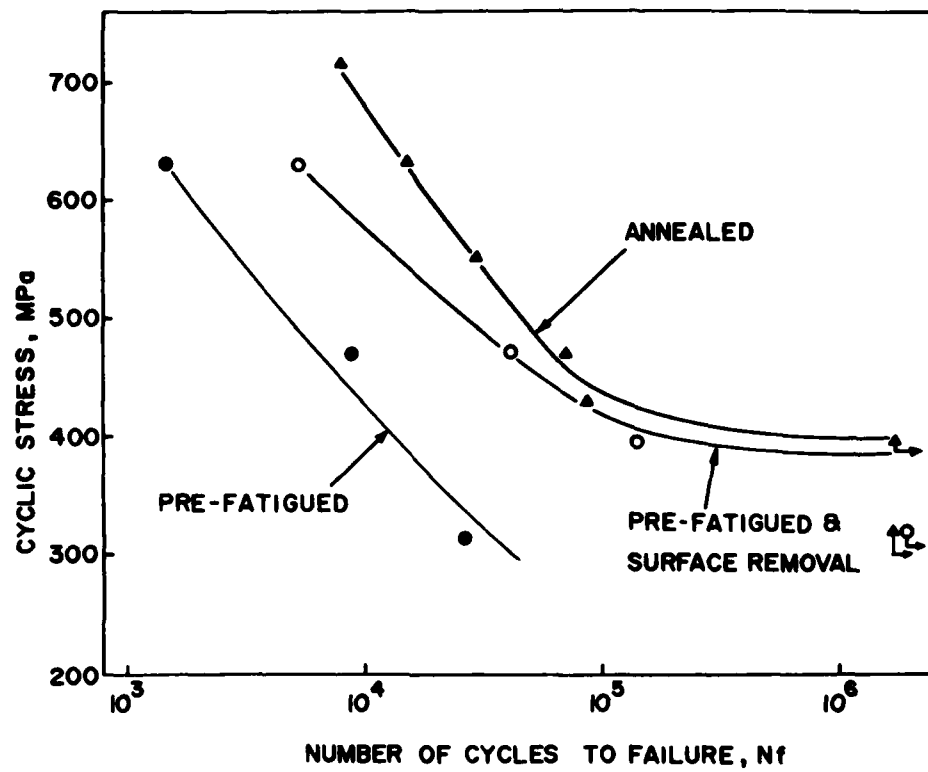


Figure 28. Effect of Pre-Fatigue Damage and Removal of Surface Layer on Fatigue Life of Ti-6Al-4V. $f=10$ Hz, $R=-1.0$.

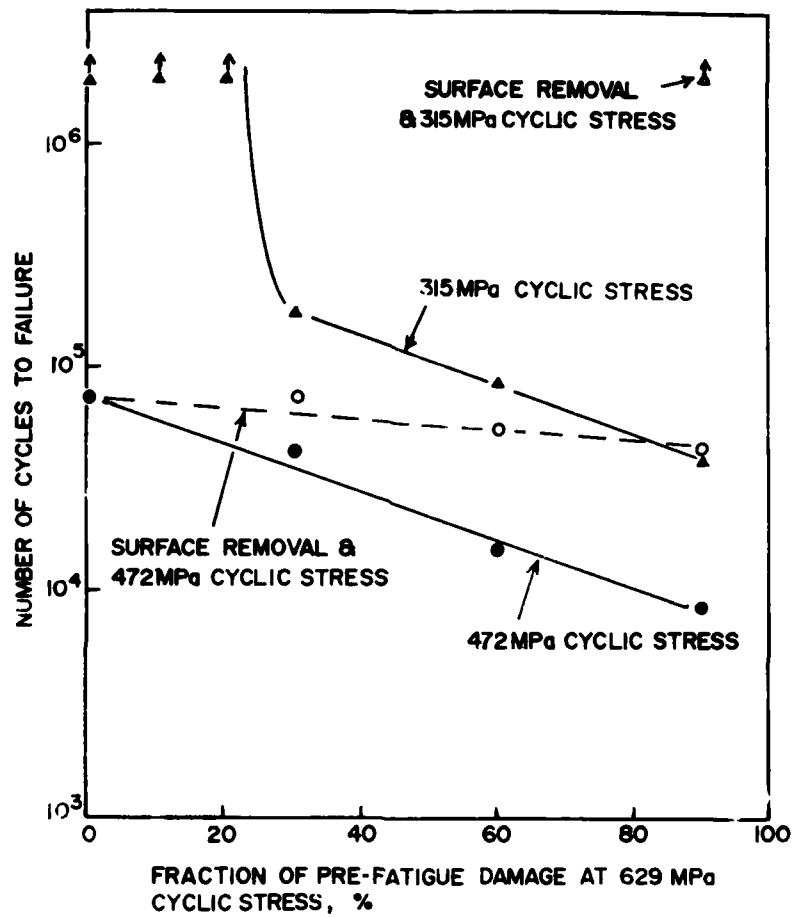


Figure 29. Dependence of Number of Cycles to Failure on Fraction of Pre-Fatigue Damage and on Surface Removal.

629 MPa and subsequently cycled at 315 MPa, failures did not occur up to 2×10^6 cycles. Consequently, pre-fatigue cycling up to about 25 pct of the life at 629 MPa has no noticeable effect on the endurance limit of the alloy.

As may have been expected from previous investigations,^{4,8} the removal of the surface layer to a depth of 100 μm essentially restored the fatigue life of the specimen fatigued 90 pct of its life at 629 MPa. The open circles in Figure 28 refer to the data points of the curves obtained after surface layer removal. Comparison with Figure 28 will show that by removal of the surface layer the accumulated damage induced by pre-fatigue cycling was eliminated. Thus, cycling with 472 MPa restored the number of cycles to failure equal to that of the original alloy without pre-fatigue cycling, and cycling with 315 MPa restored the fatigue limit.

B. Dependence of Excess Dislocation Density on Cycling and Depth Distance from Surface

X-ray rocking curve measurements of the individual grain reflections were carried out. The rocking curve gives information about the angular lattice misalignment. Since the rocking curve is a manifestation of the curvature of that lattice region over which the measurements are carried out, the measured halfwidth parameter, β , (rocking curve width at half the intensity maximum) is a measure of the excess dislocation density of one sign of the analyzed grain.^{8,12,13}

To assess the extent of lattice misalignment induced by pre-fatigue cycling with cycling stress of 629 MPa a large number of grains was analyzed. The average halfwidth value $\bar{\beta}$ of the surface grain population, as a function of the fraction of life N/N_F is given in Figure 30(a). In the DCD method the limit of resolution of measuring the angular misalignment of the grain depends on the perfection of the first crystal, that is on the β value of the monochromating silicon crystal. Using the (111) reflection of silicon the β value was 10 seconds of arc. Hence, although the lattice misalignment induced by cycling measured only a few minutes of arc, the X-ray measurements were sufficiently sensitive to reveal the dependence of $\bar{\beta}$ on N/N_F . It will be seen from Figure 30(b) that the lattice misalignment

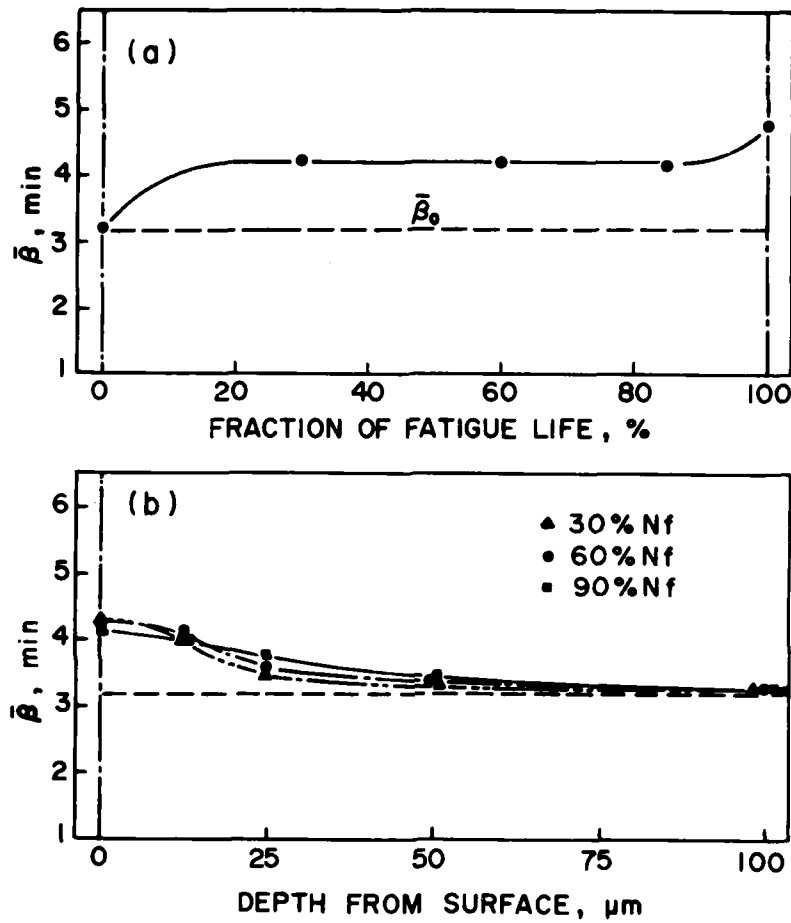


Figure 30. Dependence of Average Lattice Misalignment, $\bar{\beta}$, on (a) Fraction of Fatigue Life and (b) Depth from Surface. $f=10$ Hz, Cyclic Stress=629 MPa.

induced by pre-fatigue cycling was confined only to a surface layer of about 25 μm deep. This layer corresponded to about three grain diameters. Unlike the fatigued aluminum alloys which in the interior exhibited pronounced, induced lattice misalignment for virtually all grains at $N/N_F \sim 0.9$,⁸ the interior grains of this titanium alloy seem to be generally unaffected by the pre-fatigue cycling. It should be borne in mind, however, that highly localized cracks with concomitant lattice misalignment of adjacent grains could have developed and that these grains were not represented in the grain population analyzed by the X-ray method.

C. Slip Morphology and Dislocation Distribution

Details of the slip morphology and dislocation distribution induced by fatigue were studied by transmission electron microscopy. To ascertain the deformation response characteristic for fatigue and to establish a basis of comparison, uniaxial tension experiments were also performed. Figure 31 exhibits a typical dislocation distribution of the surface region obtained from a specimen tensile deformed to a plastic strain of $\epsilon_p = 2.7$ pct. It may be seen that the slip mode was planar. The slip bands were quite uniformly distributed in the surface as well as in the interior. The $[2\bar{1}\bar{1}0]$ slip was principally restricted to the α -phase and it may be seen from Figure 32 that the β -phase remained unaffected by the slip activity of the α -phase. By contrast, the specimen, fatigued under load control at 629 MPa to $N_F \sim 14,000$, exhibited in the surface region only localized slip activity in the α -phase. Figure 33 shows the dislocation configuration of a localized slip band. Slip in the α -phase appears to end at the β -phase and, as shown by large arrow, the α/β interphase region displayed a large accumulation of dislocations which appears to be a precursor of a microcrack. Microcracks could propagate in the α -phase and slip bands in the α -phase with contrast effects of microcrack formation such as in Figure 34 were frequently observed. Extensive TEM studies to ascertain whether slip in the α -phase even at high cyclic stresses could propagate in the β -phase showed that such slip accommodation could not be established.

In agreement with the X-ray studies no slip activity could be detected in the interior of the specimens.



Figure 31. Typical Planar Dislocation Configuration of Surface Layer, Induced by Uniaxial Tensile Deformation; $\epsilon_p = 2.7$ pct.

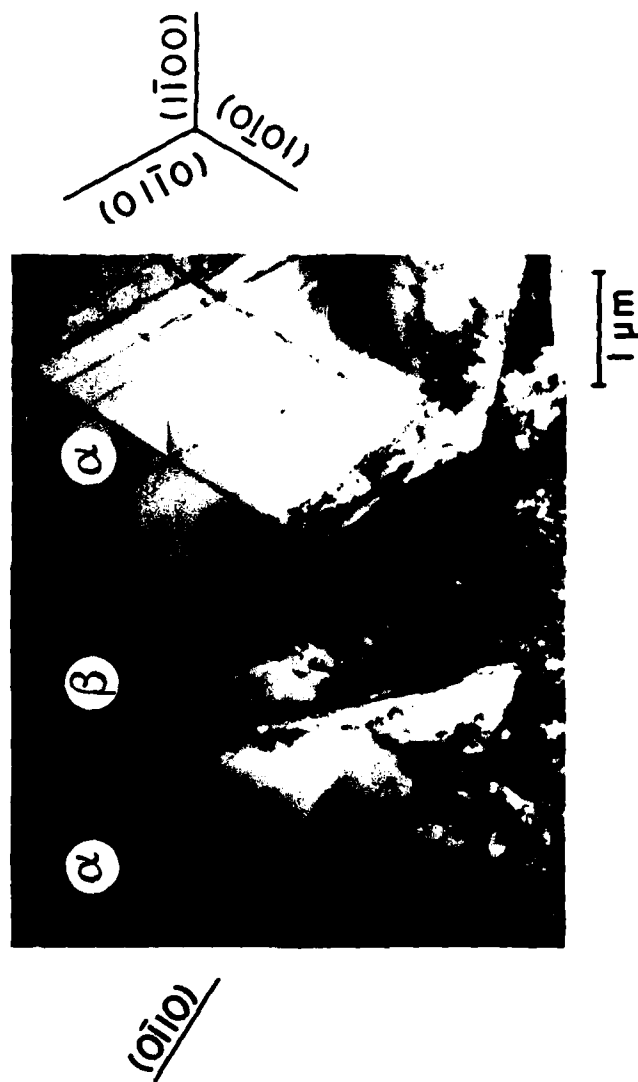


Figure 32. Slip Activity in Surface Layer Induced by Uniaxial Tensile Deformation; $\epsilon_p = 2.7$ pct.

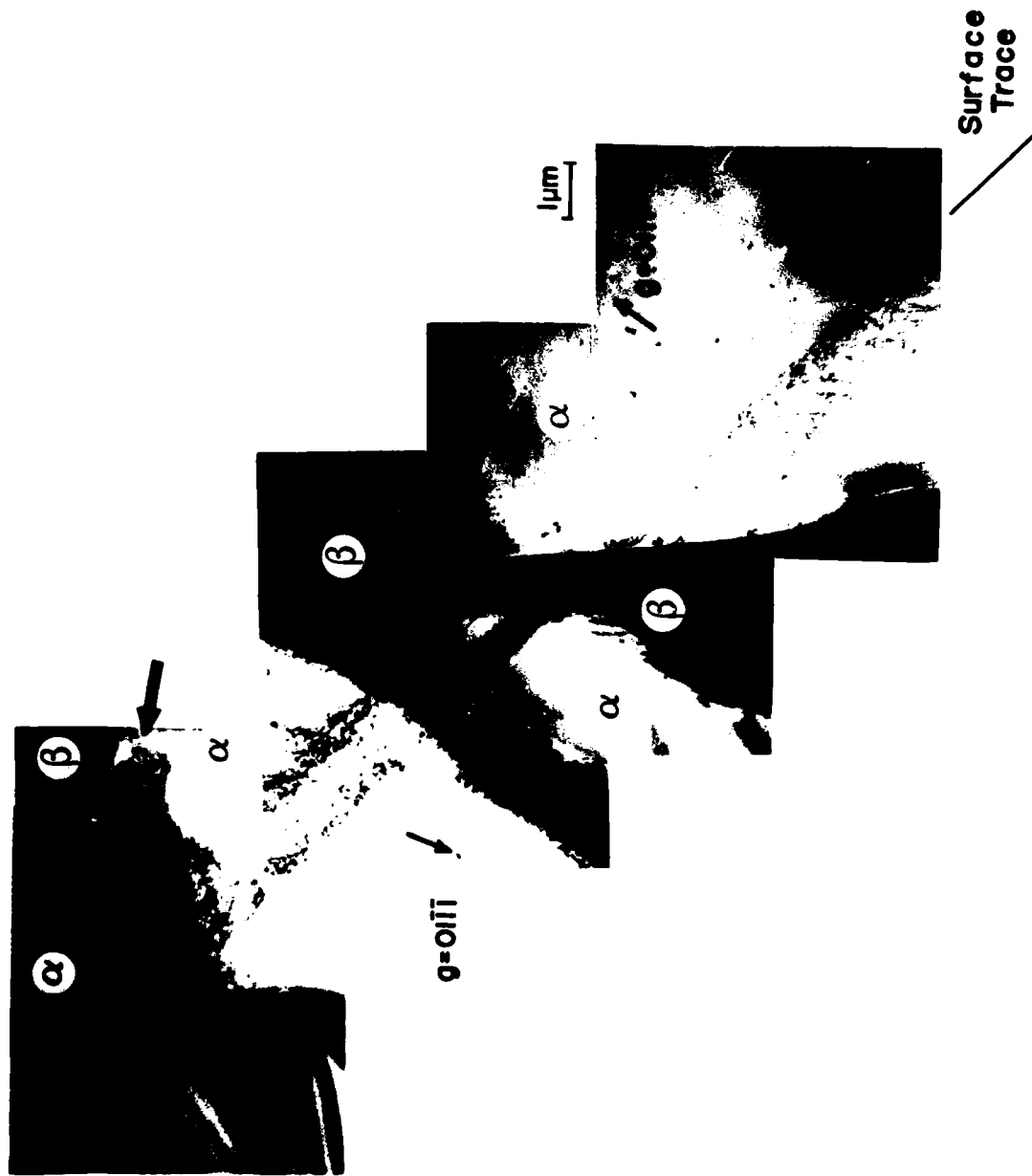


Figure 33. Dislocation Configuration of Localized Slip Band in Surface Layer, Induced by Fatigue. Cyclic Stress=629 MPa, $N_F=14,000$ cycles.

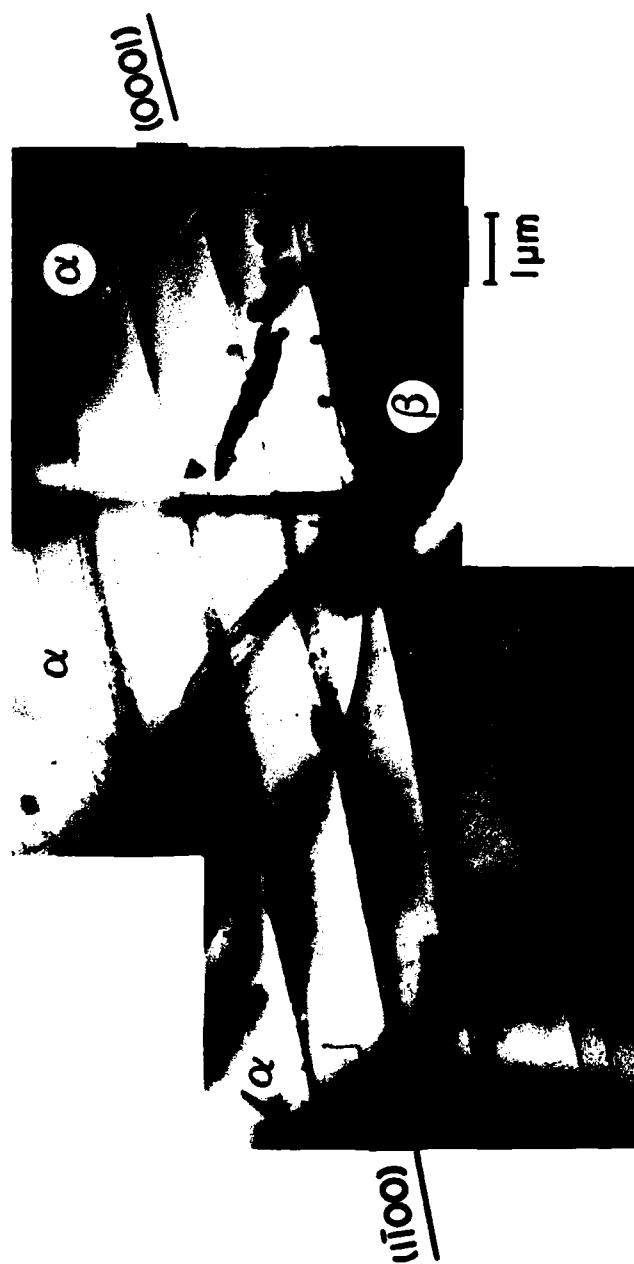


Figure 34. Localized Slip Activity in Surface Layer of α -Phase Showing Contrast Effects Characteristic of Microcracks. Cyclic Stress=629 MPa, $N_F=14,000$ cycles.

D. Observations on Crack Formation and Crack Initiation Induced by Fatigue

Investigations by scanning electron microscopy were carried out to locate the sites where fracture has been initiated. The results obtained showed that in all cases the cracks were initiated at surface sites and that secondary cracks were formed ahead of the advancing primary crack. Figure 35(a) may serve as a typical example. It gives an overall view of the fracture surface for an alloy fatigued to failure ($N_F=13,000$ cycles) at a cyclic stress of 629 MPa. The crack was initiated at the site marked by letter I. Figure 35(b) gives an enlarged view of area A exhibiting secondary cracks, some of which are marked by arrows. Virtually identical scanning electron micrographs were obtained for all alloys investigated when cycled to failure at various stress levels after prefatiguing and subsequent surface removal.

III. DISCUSSION AND CONCLUSIONS

The studies have demonstrated that in cycled Ti-Al-4V alloys the nucleation as well as the critical accumulation of fatigue damage is confined to a surface layer of about 25 μm . It has been shown that the established fatigue limit referred to an original alloy loses its significance if the alloy was subjected to a precycling treatment with a high stress amplitude viz. 80 or 90 pct of the static yield stress (Figures 28 and 29).

The cycling with a stress amplitude significantly below the fatigue limit after precycling showed a dependence of the logarithmic number of cycles to failure on the fraction of pre-fatigue damage (Figure 29). By contrast, a recent study of a cycled Al 2024 alloy which was shown to accumulate fatigue damage by a different dislocation mechanism in surface layer and interior⁸ did not show any curtailment of life when a cyclic stress below the fatigue limit was applied after severe precycling. Depending on the severity of precycling and on the magnitude of the applied cyclic stress it was shown that the accumulated fatigue damage in the titanium alloy could be either partially or totally eliminated by surface removal (Figures 28 and 29). It may be seen, however, from Figure 28 that

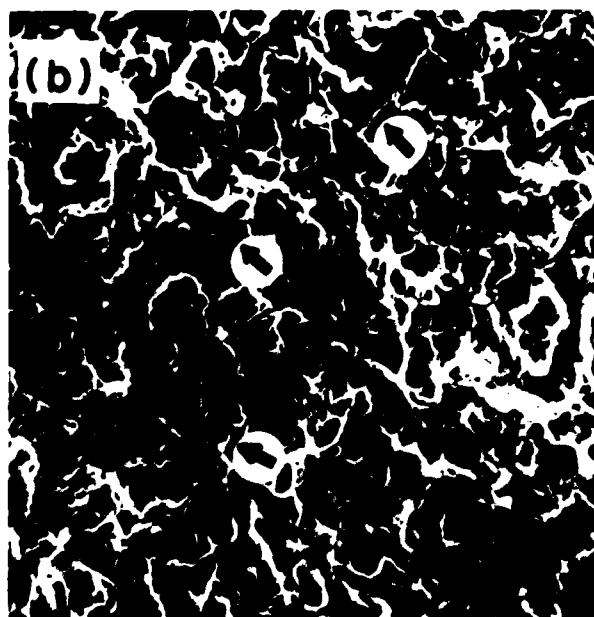
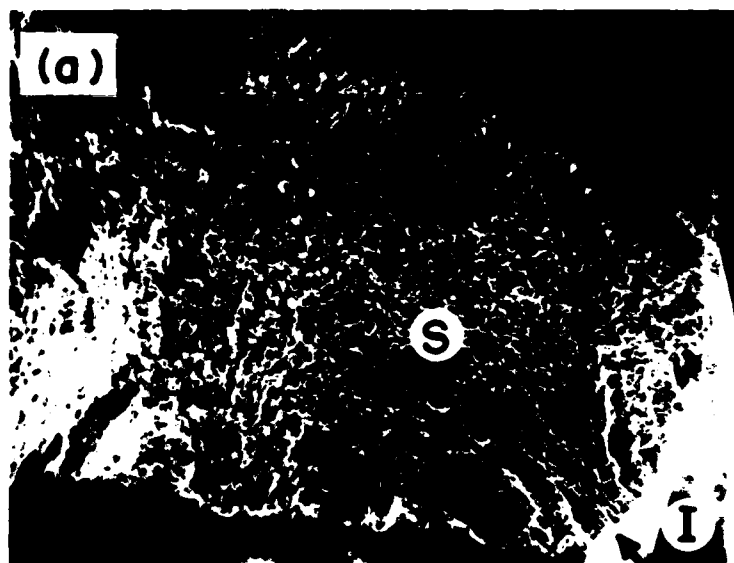


Figure 35. Fracture Surface of Ti-6Al-4V; Cyclic Stress=629 MPa, $N_F=13,000$ cycles.
 (a) Overall View, I=Crack Initiation Site
 (b) Enlarged View of Area S Exhibiting Secondary Cracks.

if the applied cyclic stress after surface removal was large, e.g., 629 MPa, the extension of the fatigue life by surface removal was by far not as efficient than when the applied stress was low. This observation suggests that very few highly localized microcracks may have formed during pre-fatigue cycling when the cyclic stress was large, viz. 629 MPa, and they may have extended beyond the 100 μm surface layer. Large cyclic stresses applied after surface removal of 100 μm contributed presumably to the enhancement of crack propagation because for such high stress levels the stress intensity factor at the crack tip is large. In order to detect the development of such localized microcracks by the X-ray DCD method through its manifestation of associated lattice misalignment, a great many more grains covering the entire gauge length would have to be analyzed than was hitherto possible. However, application of a recently developed extension of the X-ray method,^{14,15} using a position-sensitive detector with interactive computer control instead of a photographic film, should make it possible to detect such highly localized, damaged grains because of the increased ability to survey a much larger grain population. Such investigations are presently in progress. Unlike the observations made by Ruppen et al.,²⁹ and by other investigators³⁰⁻³³ who found that the origins of fatigue damage in titanium alloys are often located at subsurface sites of several hundred micrometers, this investigation has found the origins of fatigue damage intimately associated with a surface layer of less than 100 μm . In agreement, however, with the studies of Ruppen et al., the present investigation found also crack initiation sites to be located predominantly at the α/β interphase region as a result of dislocation-microstructural interaction, a consideration initially raised by Neal and Blenkinsop.³¹ The TEM investigations of this study, however, were unable to reveal in the fatigued alloy any correlation of slip compability between the α and β phases as postulated by Ruppen et al.²⁹ In the absence of slip accommodation in the β phase which represents only 10 pct of the two-phase alloy, the β phase may be considered to play the role equivalent to hard inclusions embedded in the α -phase. Slip activity in the softer α -phase would result in characteristic dislocation pile-ups at the α/β interphase such as that shown in Figure 33 and identical ones reported by other investigators.^{29,31} Mechanisms of crack formation involving the interaction of dislocations moving on several prism planes at the α/β interphase

region, as proposed by Ruppen et al.,²⁹ could account for the crack initiation stage in the surface layer.

IV. SUMMARY

1. Fatigue life and fatigue limit in Ti-6Al-4V were strongly dependent on the severity of precycling.
2. The fatigue limit disappeared if the alloy was subjected to a precycling treatment with a high stress amplitude.
3. The number of cycles to failure at low stress amplitudes exhibited a logarithmic dependence on the fraction of pre-fatigue damage.
4. The interdependence of fatigue life and fatigue limit to precycling history was attributed to microcrack formation developed in a surface layer of less than 100 μm .
5. The fatigue damage could be either partially or totally eliminated by removal of the surface layer.
6. The α/β interphase region of the surface layer appeared to be the preferred sites for dislocation pile-ups and crack initiation.

REFERENCES

1. H. Shen, S. E. Podlaseck and I. R. Kramer, Trans, Met. Soc., AIME 233, 1933 (1965).
2. H. Shen and I. R. Kramer: Fatigue in Vacuum Environment, Trans. Int. Vacuum, Met. Conf. 236 (1967).
3. I. R. Kramer, Proc. Air Force Conf. on Fatigue, AFCDL-TR-0-144 (1969).
4. I. R. Kramer, Met Trans. 5, 1735 (1974).
5. B. I. Verkin and N. M. Grinberg (Review Paper) Mat. Sci. and Eng. 41, 149 (1979).
6. R. N. Pangborn, S. Weissmann and I. R. Kramer, Fatigue Failure Prediction by X-ray Double Crystal Diffractometry and Topography, Strength of Metals and Alloys, Pergamon Press, New York, 1979, p. 1279.
7. R. N. Pangborn, S. Weissmann and I. R. Kramer, Determination of Pre-fracture Fatigue Damage, Report No. DTNSRDC-80/006 (Jan. 1980).
8. R. N. Pangborn, S. Weissmann and I. R. Kramer, Met. Trans. 12A, 109 (1981).
9. T. H. Sanders, Jr., and J. T. Staley, Review of Fatigue and Fracture Research on High-Strength Aluminum Alloys, Fatigue and Microstructure, ASM, 467 (1979).
10. C. H. Wells and C. P. Sullivan, ASM Trans. 57, 541 (1964).
11. D. K. Benson, I. C. Grosskreutz and G. G. Shaw, Met. Trans. 3, 1239 (1972).
12. S. Weissmann, J. Appl. Phys. 27, 389 (1956).
13. S. Weissmann, Trans. ASM 52, 599 (1960).
14. R. Yazici, W. Mayo, T. Takemoto and S. Weissmann, Defect Structure Analysis of Polycrystalline Materials by Computer Controlled Double Crystal Diffractometer and Position Sensitive Detector, XII Cong. of Int. Union of Cryst., Ottawa, Canada, Aug. 1981, pp. 16-25.
15. W. E. Mayo, Study of Microscopic Strain Distributions in Metal Systems, Ph.D. Thesis, Jan. 1982, Rutgers University, New Brunswick, N.J.
16. D. J. Duquette, Environmental Effects I: General Fatigue Resistance and Crack Nucleation in Metals and Alloys, Fatigue and Microstructure, ASM (1979) 335.
17. C. A. Stubbington, Metallurgia 68, 109 (1963).
18. P. J. E. Forsyth, Acta Met. 11, 703 (1963).
19. R. E. Stoltz and R. M. Pelloux, Met. Trans. 3, 2433 (1972).

20. T. Broom and A. Nicholson, J. Inst. Metals 89, 183 (1960).
21. J. H. Shively, R. F. Hehemann and A. R. Troiano, Corrosion 22, 253 (1966).
22. L. V. Corsetti and D. J. Duquette, Met. Trans. 5, 1087 (1974).
23. R. J. Jacko and D. J. Duquette, Met. Trans. 8A, 1821 (1977).
24. M. O. Speidel, Hydrogen in Metals, Proc. of Int. Conf. on the Effects of Hydrogen on Materials Properties (1973) 249.
25. R. P. Wei, Int. J. Frac. Mech. 5, 71 (1969).
26. J. K. Tien, Effects of Hydrogen on Behavior of Materials, A. W. Thompson and I. M. Bernstein, eds. AIME, N.Y. (1976) 309.
27. H. H. Johnson and J. P. Hirth, Met. Trans. 7A, 1543 (1976).
28. K. Endo, K. Komai and J. Watase, J. Mater. Sci., Japan. 24, 1140 (1975).
29. J. Ruppen, P. Bhowal, D. Eylon and A. J. McEvily, Fatigue Mechanisms, ASTM, Philadelphia, Pa. (1979) 47.
30. R. K. Steele and A. J. McEvily, Engineering Fracture Mechanics 8, 31 (1976).
31. D. F. Neal and P. A. Blenkinsop, Acta Met. 24, 59 (1976).
32. D. Eylon and J. A. Hall, Met. Trans. A, 8A, 981 (1977)
33. R. Chait and T. S. DeSisto, Met. Trans. A, 8A, 1017 (1977)

INITIAL DISTRIBUTION

Copies

2 CNR
1 Code 465
1 Code 471

4 NRL
1 Code 6300
1 Code 6311
1 Code 6380
1 Code 6385

2 NAVAIR (AIR 320)

1 Naval Air Development Center
Naval Materials Center
Warminster, PA 18974
Attn: Dr. F.W. Williams
(Code 606)

5 NAVSEA
1 SEA 035
1 SEA 05D
1 SEA 323
2 SEA 99612

12 DTIC

1 Air Force Materials Laboratory
Wright-Patterson AF Base
Dayton, OH 45433
(Attn: Dr. H. Burte)

1 National Bureau of Standards
Washington, DC 20234
(Attn: Dr. Jerome Kruger)

1 Case Western Reserve
Mechanical and Aerospace
Engineering
Cleveland, OH 44106
(Attn: S.S. Manson)

1 University of Connecticut
Storrs, CT 06268
(Attn: Dr. A.J. Evily)

2 Johns Hopkins University
School of Engineering
Baltimore, MD 21218
(Attn: Dr. R. Green, R. Pond)

Copies

1 Lehigh University
32/ Sinclair Lab., Bldg 7
Bethlehem, PA 18015
(Attn: Dr. R.P. Wei)

1 University of Maryland
Dept. of Chemical Eng.
College Park, Md. 20740
(Attn: Dr. R. Arsenault)

3 Massachusetts Institute of
Technology
Cambridge, MA 02139
(Attn: Dr. R. Latanison,
Dr. N. Saka, and
Dr. M. Cohen)

1 Northwestern University
Evanston, IL 60201
(Attn: Dr. J. B. Cohen)

1 Ohio State University
Met. Engr. Dept.
116 W. 19th Avenue
Columbus, OH 43210
(Attn: John P. Hirth)

1 Polytechnic Inst of New York
333 Jay Street
Brooklyn, NY 11201
(Attn: Dr. H. Margolin)

1 Rensselaer Polytechnic Inst
Troy, NY 12181
(Attn: Dr. D.J. Duquette)

1 University of Rochester
Dept. of Mechanical Engr.
Rochester, NY 14627
(Attn: Dr. James C. Li)

10 Rutgers University
Piscataway, NJ 08854
(Attn: Dr. W. Weissmann)

Copies

2 Syracuse University
Link Hall
Syracuse, NY 13210
(Attn: Dr. Y. Oshida)
Dr. Volker Weise

1 University of Virginia
Dept. of Applied Sciences
Charlottesville, VA 22904
(Attn: Dr. D. K. Wilsdorf)

1 Carnegie-Mellon University
Pittsburgh, PA 15213
(Attn: Dr. J.C. Williams)

2 University of Illinois
Dept. of Met. & Min. Eng.
Urbana, IL 61801
(Attn: Dr. H.K. Birnbaum and
Dr. C. Altstetter)

CENTER DISTRIBUTION

Copies	Code
2	012
2	17
1	28
1	280
15	2802
2	281
6	282
10	5211.1 Rept Dist
1	522.1 Library (C)
1	522.2 Library (A)
2	5231 Office Services

DTNSRDC ISSUES THREE TYPES OF REPORTS

- 1. DTNSRDC REPORTS, A FORMAL SERIES, CONTAIN INFORMATION OF PERMANENT TECHNICAL VALUE. THEY CARRY A CONSECUTIVE NUMERICAL IDENTIFICATION RELAYED ON THEIR CLASSIFICATION OR THE ORIGINATING DEPARTMENT.**
- 2. DEPARTMENTAL REPORTS, A SEMI-FORMAL SERIES, CONTAIN INFORMATION OF A PERMANENT, TEMPORARY, OR PROPRIETARY NATURE OR OF LIMITED INTEREST OR SIGNIFICANCE. THEY CARRY A DEPARTMENTAL ALPHANUMERICAL IDENTIFICATION.**
- 3. TECHNICAL MEMORANDA, AN INFORMAL SERIES, CONTAIN TECHNICAL INFORMATION OF LIMITED USE AND INTEREST. THEY ARE PRIMARILY WORKING PAPERS INTENDED FOR INTERNAL USE. THEY CARRY AN IDENTIFYING NUMBER WHICH INDICATES THEIR TYPE AND THE NUMERICAL CODE OF THE ORIGINATING DEPARTMENT. ANY DISTRIBUTION OUTSIDE THE DTNSRDC MUST BE APPROVED BY THE HEAD OF THE ORIGINATING DEPARTMENT ON A CASE-BY-CASE BASIS.**

DATE
ILMEI
—8